

# Systematic Uncertainties in Black Hole Masses Determined from Single Epoch Spectra

Kelly D. Denney<sup>1</sup>, Bradley M. Peterson<sup>1</sup>, Matthias Dietrich<sup>1</sup>, Marianne Vestergaard<sup>2</sup>, and Misty C. Bentz<sup>1,3</sup>

## ABSTRACT

We explore the nature of systematic errors that can arise in measurement of black hole masses from single-epoch spectra of active galactic nuclei (AGNs) by utilizing the many epochs available for NGC 5548 and PG1229+204 from reverberation mapping databases. In particular, we examine systematics due to AGN variability, contamination due to constant spectral components (i.e., narrow lines and host galaxy flux), data quality (i.e., signal-to-noise ratio,  $S/N$ ), and blending of spectral features. We investigate the effect that each of these systematics has on the precision and accuracy of single-epoch masses calculated from two commonly-used line-width measures by comparing these results to recent reverberation mapping studies. We calculate masses by characterizing the broad H $\beta$  emission line by both the full width at half maximum and the line dispersion and demonstrate the importance of removing narrow emission-line components and host starlight. We find that the reliability of line width measurements rapidly decreases for  $S/N$  lower than  $\sim 10$  to 20 (per pixel) and that fitting the line profiles instead of direct measurement of the data does not mitigate this problem but can, in fact, introduce systematic errors. We also conclude that a full spectral decomposition to deblend the AGN and galaxy spectral features is unnecessary except to judge the contribution of the host galaxy to the luminosity and to deblend any emission lines that may inhibit accurate line width measurements. Finally, we present an error budget which summarizes the minimum observable uncertainties as well as the amount of additional scatter and/or systematic offset that can be expected from the individual sources of error investigated. In particular, we find that the minimum observable uncertainty in single-epoch mass estimates due to variability is  $\lesssim 0.1$  dex for high  $S/N$  ( $\gtrsim 20$  pixel<sup>-1</sup>) spectra.

---

<sup>1</sup>Department of Astronomy, The Ohio State University, 140 West 18th Avenue, Columbus, OH 43210; denney, bentz, dietrich, peterson@astronomy.ohio-state.edu

<sup>2</sup>Department of Physics and Astronomy, Tufts University, Medford, MA 02155; m.vestergaard@tufts.edu

<sup>3</sup>Present address: Dept. of Physics and Astronomy, 4129 Frederick Reines Hall, University of California at Irvine, Irvine, CA 92697-4575; mbentz@uci.edu

*Subject headings:* galaxies: active — galaxies: nuclei — galaxies: black holes

## 1. INTRODUCTION

Understanding the demographics of supermassive black holes (BHs) is imperative to expanding our understanding of the present state as well as the cosmic evolution of galaxies. In particular, links between BHs and properties of host galaxies point to coevolution (Kormendy & Richstone 1995; Ferrarese & Merritt 2000; Gebhardt et al. 2000a). This is a surprising conclusion, given the small sphere of influence of the central BH compared to the size of the galaxy. To trace the cosmic evolution of BHs, we must determine BH masses as a function of cosmic time, thus requiring the measurement of BH masses at large distances. The direct methods (e.g. stellar and gas dynamics, megamasers) that have succeeded for  $\sim 30 - 40$  comparatively local, mostly quiescent galaxies (see review by Ferrarese & Ford 2005) fail at large distances because they require high angular resolution to resolve motions within the radius of influence of the BH. A solution to this distance problem is to use AGNs as tracers of the BH population at redshifts beyond the reach of the above mentioned methods. AGNs are luminous and easier to observe than quiescent galaxies at large distances. Most importantly, their masses can be determined by reverberation mapping (Blandford & McKee 1982; Peterson 1993), a method that does not depend on angular resolution.

Masses have been measured for nearly 40 active galaxies with reverberation mapping (RM) methods (see the recent compilation by Peterson et al. 2004). The results of these studies have led to the identification of certain scaling relationships for AGNs. The correlation between BH mass and bulge/spheroid stellar velocity dispersion, i.e. the  $M_{\text{BH}} - \sigma_{\star}$  relation, for AGNs (Gebhardt et al. 2000b; Ferrarese et al. 2001; Onken et al. 2004; Nelson et al. 2004) is consistent with that discovered for quiescent galaxies (Ferrarese & Merritt 2000; Gebhardt et al. 2000a; Tremaine et al. 2002). In addition, and more relevant for this study, is the correlation between the broad-line region (BLR) radius and the luminosity of the AGN, i.e. the  $R - L$  relation (Kaspi et al. 2000, 2005; Bentz et al. 2006, 2008), which allows estimates of BH masses from single-epoch (SE) spectra. This relation affords great economy of observing resources, allowing masses to be calculated for the large number of AGNs/quasars with SE spectra obtained from surveys such as the SDSS and AGES (e.g., Vestergaard 2002; Corbett et al. 2003; Vestergaard 2004; Kollmeier et al. 2006; Vestergaard et al. 2008; Shen et al. 2008a,b; Fine et al. 2008).

Measuring BH masses from single-epoch spectra presents itself as a remarkably powerful tool for determining black hole masses at all redshifts for potentially all spectroscopically observed quasars. However, many effects limit the precision of these measurements, the most

important being how well the emission-line widths represent the true motions of the BLR gas — for example, if the BLR has a flattened disk-like geometry, the unknown inclination of the system can result in a huge uncertainty in the mass (Collin et al. 2006). For the moment, however, if we set aside the issue of these calibration uncertainties (i.e., the accuracy of the RM measurements themselves), the relevant question becomes: how well can the SE mass measurements reproduce the RM measurements? Scaling relationships are being used with increased frequency in the literature to indirectly measure black hole masses from single-epoch spectra. Therefore, it is imperative that we understand the systematic uncertainties introduced in measuring a SE black hole mass. In particular, there are four systematics we will discuss that clearly affect how well SE mass estimates reproduce the RM measurements of BH masses.

1. **Variability:** The most inherent and unavoidable systematic in measuring masses of AGNs is intrinsic variability that causes the luminosity, line widths, and reverberation lag to change with time. The variable luminosity leads to variable BLR radius determinations when the  $R - L$  relation is used, so we are therefore likely to measure different SE masses for different epochs. In the case of AGNs for which multiple measurements of line widths and radii are available from reverberation studies, the relationship between line width and BLR radius (i.e. reverberation lag) is consistent with a virial relationship,  $\Delta V \propto R^{-1/2}$  (Peterson & Wandel 1999, 2000; Onken & Peterson 2002; Kollatschny 2003), as expected if the BLR dynamics are dominated by gravity. This relationship also seems to hold at least approximately for individual emission lines measured at different times (e.g. Peterson et al. 2004): the size of the BLR as measured in a particular emission line scales with luminosity approximately as  $R \propto L^{1/2}$  so we would expect that the line width would correspondingly decrease as  $\Delta V \propto L^{-1/4}$  in order to preserve the virial relationship. Evidence to date suggests that the central mass deduced from reverberation experiments at different epochs is constant or, at worst, a weak function of luminosity (Collin et al. 2006). This is itself quite remarkable since we are characterizing a region that is undoubtedly rather complex (cf. Elvis 2000) by two quantities, the average time for response of an emission line to continuum variations and the emission-line width. In a previous investigation of variability on SE mass measurements using CIV  $\lambda 1549$  emission, Wilhite et al. (2007) show that the distribution of fractional change in  $M_{\text{BH}}$  between epochs for several hundred SDSS quasars has a dispersion of  $\sim 0.3$ . Only part of this dispersion can be accounted for by random measurement errors. Similarly, Woo et al. (2007) estimate the uncertainty in SE mass measurements based solely on propagating the variability in the measurement of the  $\text{H}\beta$  FWHM. They demonstrate that the uncertainty is roughly 30%. However, the  $S/N$  of their data was low ( $\sim 10 - 15 \text{ pixel}^{-1}$ ), and they attribute a large fraction

of their measured uncertainty to random measurement errors in the line width. Here we will investigate the effect of variability by determining the consistency of masses based on the two observables from optical SE spectra: the monochromatic luminosity at  $5100\text{\AA}$  and the  $H\beta$  line width. We will use several hundred spectra of the Type 1 AGN NGC 5548 and a smaller sample of spectra of the Palomar Green (PG) quasar PG1229+204.

2. **Contamination by Constant Components:** The variable AGN spectrum is contaminated by relatively constant components. These include narrow emission lines and host galaxy starlight. As the AGN luminosity varies, so does the relative contributions to the observed spectrum from these sources. We will determine how the SE mass measurements are affected by these non-variable features in the spectrum. In particular, we will examine changes in the precision and accuracy of the masses when these contaminating features remain in the spectrum, compared to when their contributions are subtracted before luminosities and line widths are measured.
3. **Signal-to-Noise Ratio:** Accurately measuring the spectroscopic properties needed for calculating the SE mass is highly dependent on the quality of the spectra. This is particularly true for measuring emission-line widths. Certainly not all spectra used for such calculations in the literature are of comparable quality. Therefore, we will demonstrate how changes in the signal-to-noise ratio ( $S/N$ ) of the data affect SE mass measurements. To make this comparison, we will artificially degrade the  $S/N$  of our sample to various levels and compare the resulting masses. In addition, it is common practice (e.g., McLure & Dunlop 2004; Woo et al. 2007; Shen et al. 2008b; McGill et al. 2008) to fit functions to emission-line profiles in data with comparatively low  $S/N$  in the hopes of yielding more accurate line-width measurements. Here we test the usefulness of this practice by calculating and comparing SE masses using line widths measured directly from the data to those using line widths measured from fits to the line profiles of the original and  $S/N$ -degraded spectra.
4. **Blending:** The optical region of broad-line AGNs is often characterized by blending from many broad emission features as well as contributions from the host galaxy starlight and AGN thermal emission. Therefore, detailed modeling and decomposition of a spectrum into individual spectral components is useful for isolating the features required for accurately measuring SE masses. However, this process is rather time consuming as well as non-unique, since it requires assumptions about the types of templates to fit and the relative contributions to fit for each SE spectrum. Instead, to make SE mass measurements for a large number of AGNs, it is expedient to use simple algorithms or prescriptions for these measurements. There is concern, however, that AGN

emission-line blending and host galaxy features can affect the accuracy of the line width measurements that utilize these simple prescriptions. With these considerations in mind, we will compare SE mass measurements made from measuring spectral properties using a simple prescription for local continuum fitting and subtraction versus detailed modeling and decomposition of the optical region to remove any extraneous components.

This is not a comprehensive list of systematics, but these particular issues have a common element: all can be addressed empirically using a large number of SE spectra of a single variable source. The use of a single source (actually, two single sources) is what sets this study apart from past investigations, particularly on the point of understanding the effect of variability on SE masses. This is an important distinction, given that Kelly & Bechtold (2007) show that an intrinsic correlation between  $M_{\text{BH}}$  and  $L$  that is statistically independent of the  $R-L$  relationship (supported by, e.g. Corbett et al. 2003; Netzer 2003; Peterson et al. 2004) can lead to an artificially broadened SE mass distribution when it is composed of masses from multiple sources. They suggest that because of this intrinsic  $M_{\text{BH}} - L$  relation, using the luminosity simply as a proxy for the BLR radius may cause additional scatter in the mass estimates because additional information about the BH mass that may be contained in  $L$  is ignored. By utilizing many epochs from the same object, however, the effect on SE masses due strictly to variability can be isolated, while the broadening caused by a possible  $M_{\text{BH}} - L$  correlation is avoided, because we are dealing with a single black hole mass. Therefore, any additional information about  $M_{\text{BH}}$  contained in the luminosity could only affect the overall accuracy of our SE measurements, not the scatter in our mass distributions due to variability.

For each of the potential sources of uncertainty listed above, we consider the effect on the precision of the SE mass estimates, which is determined from the dispersion of these masses about the mean sample value. We will also consider the accuracy of the SE measurements, which we define as the systematic offset between the distribution average and a single mass based on reverberation mapping results for the same sample. We are not, however, addressing the accuracy of the reverberation mapping masses themselves. Better understanding and quantifying the systematic uncertainties and zero-point calibration of the reverberation mapping mass scale is an important but difficult endeavor and will therefore be the focus of future work. Because the focus of this paper is not the accuracy of the RM measurements but instead on the reproducibility of these values by SE measurements, we will work only with the virial product, given by

$$M_{\text{vir}} = \frac{c\tau(\Delta V)^2}{G}, \quad (1)$$

where  $\tau$  is the measured time delay between the continuum and broad emission-line variations (so that  $c\tau$  is the effective BLR radius) and  $\Delta V$  is the velocity dispersion of the BLR gas. Here, we measure the velocity dispersion from the width of the broad  $H\beta$  emission line. By dealing simply with the virial product, or virial mass, we bypass the zero-point calibration issue with the actual black hole mass<sup>1</sup>,  $M_{\text{BH}}$ . In addition, we will consider without prejudice the two common measures for characterizing line widths: the full width at half maximum (FWHM) and the line dispersion, or second moment of the line profile,  $\sigma_{\text{line}}$ .

## 2. Data and Analysis

### 2.1. NGC 5548 Spectra

The extensive, multi-decade monitoring of the Seyfert 1 galaxy NGC 5548 has led to one of the largest collections of observations of any single AGN. The size of this data set alone makes this object an obvious choice for studying SE mass measurements. The spectra of NGC 5548 for this paper were selected from the International AGN Watch public archives<sup>2</sup>. With spectral quality in mind, we choose several subsets of the available 1494 spectra for the different analyses within this paper. In our analysis of AGN variability and the effects due to the constant spectral components in §§3.1 and 3.2, we use a total of 370 spectra, including the “Revised selected optical spectra (1989-1996)” covering years 1–5 (Wanders & Peterson 1996), as well as the remaining spectra from the 1.8m Perkins Telescope at Lowell Observatory covering years 6 – 10 (Peterson et al. 1999, 2002). This subset of data represents a nearly homogeneous set of high-quality spectra that is centered on the  $H\beta$   $\lambda 4861$  region of the optical spectrum. We then use a smaller subset of this NGC 5548 data set for the  $S/N$  analysis in §3.3, separating from the 370 spectra only those 270 observations made with the Perkins Telescope. These 270 spectra were all obtained with the same instrument and instrumental setup, which kept properties such as the entrance aperture, spectral resolution, and wavelength range nearly constant for all observations. This sample allows us to target the systematic errors due to changes in  $S/N$  rather than additional observational systematics. For the analysis of spectral component blending covered in §3.4, we focus on a set of 33 spectra from years 6 – 13 of the AGN Watch campaign (Peterson et al. 1999, 2002) observed with the 3.0m Shane Telescope at Lick Observatory. These spectra have full optical wavelength coverage spanning rest frame  $\sim 3000 - 7000 \text{ \AA}$ . Utilizing this wide

---

<sup>1</sup>This mass can be determined by scaling  $M_{\text{vir}}$  by a factor,  $f$ , which accounts for the unknown BLR geometry and kinematics (e.g., Onken et al. 2004; Collin et al. 2006; Labita et al. 2006; Decarli et al. 2008).

<sup>2</sup><http://www.astronomy.ohio-state.edu/~agnwatch/>

spectral coverage, we perform full AGN-host spectral decompositions using two independent methods to better judge the effects of blending.

Each of the above data sets have been internally flux calibrated to the [O III]  $\lambda 5007$  line flux in the mean spectrum using a  $\chi^2$  minimization algorithm developed by van Groningen & Wanders (1992). In this method the narrow emission-line flux can be taken as constant, since these lines arise in an extended, low density region and are thus unaffected by short timescale variations in the ionizing continuum flux. Following this internal flux calibration, all subsets were scaled to the absolute [O III]  $\lambda 5007$  line flux of  $5.58 \times 10^{-13}$  erg s $^{-1}$  cm $^{-2}$  (Peterson et al. 1991).

## 2.2. PG1229+204 Spectra

The PG quasar PG1229+204 (hereafter PG1229) from the Bright Quasar Survey was chosen as an additional object for this study because it is also a Type 1 AGN with a reverberation mapping mass measurement. In contrast to NGC 5548, however, it is a higher luminosity source where neglecting the host galaxy and narrow lines is less likely to interfere with the SE mass measurement. In addition, results for this object will allow for a more meaningful comparison (than the low-luminosity Seyfert 1 NGC 5548) with other quasars for which the  $R - L$  scaling method is more relevant. The 32 optical spectra in our sample were originally published along with reverberation mapping results for several PG quasars by Kaspi et al. (2000) and reanalyzed by Peterson et al. (2004). Here, we are again interested in the  $H\beta$  region of the optical spectrum. The absolute spectral fluxes of these data were calibrated externally with comparison stars in the same field as the object (for further details see Kaspi et al. 2000).

## 2.3. Methodology for Measuring Virial Masses

### 2.3.1. Virial Masses from Single-Epoch Spectra

The virial mass can be measured from a single optical spectrum by using the width of the broad  $H\beta$  emission line as a measure of the BLR velocity dispersion and  $\lambda L_\lambda$  at  $\lambda = 5100$  Å in the rest frame as a proxy for the BLR radius,  $c\tau$ , through the use of the  $R - L$  scaling relation (e.g. Kaspi et al. 2000; Bentz et al. 2006, 2008). We use the  $R - L$  relation of Bentz et al. (2008) because it includes the most current reverberation mapping results and luminosities that have been corrected for host galaxy starlight contamination. Using this form of the  $R - L$  scaling relation and the virial mass formula given by equation

1 (i.e., excluding any assumptions about the scale factor,  $f$ ), the SE virial mass is given by

$$\log\left(\frac{M_{\text{SE}}}{M_{\odot}}\right) = -22.0 + 0.519 \log\left(\frac{\lambda L_{5100}}{\text{erg s}^{-1}}\right) + 2 \log\left(\frac{V_{\text{H}\beta}}{\text{km s}^{-1}}\right), \quad (2)$$

where  $\lambda L_{5100}$  is the luminosity at rest frame wavelength 5100 Å, and  $V_{\text{H}\beta}$  is the line width of the broad H $\beta$  emission line. SE masses have been calculated in the literature using various combinations of line widths and luminosity measurements (for examples and comparisons, see McGill et al. 2008). Therefore, we calculate eight virial masses for each SE spectrum using different combinations of line width and luminosity measurements. Through comparisons of these different mass estimates, we observe how the systematics listed above affect the resulting SE masses in relation to each of the spectral properties that we isolate in our calculation.

For the investigations of AGN variability, constant components, and  $S/N$  in §§3.1 – 3.3, the continuum flux density is taken as the average between observed-frame wavelengths 5170 Å and 5200 Å for NGC 5548 and between 5412 Å and 5456 Å for PG1229. These flux densities were corrected for Galactic extinction, and then luminosity distances were calculated assuming the following cosmological parameters:  $\Omega_m = 0.3$ ,  $\Omega_{\Lambda} = 0.70$ , and  $H_0 = 70$  km sec $^{-1}$  Mpc $^{-1}$ . Luminosities for each spectrum were calculated both from the measured continuum flux density and from the host galaxy-subtracted flux density. For NGC5548 spectra the AGN continuum was then subtracted from each spectrum based on a linearly interpolated fit between two local continuum regions: one blueward of H $\beta$  over the observed-frame range 4825 – 4840 Å and one redward of [O III]  $\lambda$ 5007 over the range 5170 – 5200 Å. Similarly, local continuum regions were defined for PG1229 over the ranges 5063 – 5073 Å and 5412 – 5456 Å.

Following continuum subtraction, H $\beta$  line widths are measured from each spectrum within the following observed-frame wavelength ranges. For the majority of the NGC 5548 data, H $\beta$  is defined over the wavelength range 4845 – 5018 Å for spectra with narrow line components still present but was extended to the range 4845 – 5036 Å for spectra from which we have removed the narrow lines because it is often clear that the H $\beta$  profile extends under the [O III]  $\lambda$ 4959 emission line. However, during year 4 of the AGN Watch campaign (JD2448636–JD2448898), NGC 5548 was in an extremely low luminosity state, thus necessitating a different choice for the H $\beta$  line boundaries and local continuum region blueward of this line. For spectra observed this year, we extended the boundaries of H $\beta$  to 4810 – 5135 Å and defined the local continuum region blueward of H $\beta$  to be between 4782 – 4795 Å. For the PG1229 data set, H $\beta$  is defined over the range 5075 – 5248 Å or 5075 – 5310 Å for spectra with and without narrow lines, respectively. We measure the line dispersion from the blue



side of the broad  $H\beta$  line,  $\sigma_{\text{blue}}$ , assuming a symmetric profile about the line center. This is done to avoid residuals from the  $[O\text{ III}]\lambda\lambda 4959, 5007$  narrow emission-line subtraction as well as possible Fe II contamination commonly present on the red side of the profile. The FWHM is measured from the full line profiles described above. The exact procedures used for measuring these line widths follow those of Peterson et al. (2004). We measure the line widths directly from the data, except in one subsection of the  $S/N$  analysis (§3.3.2), where line widths are measured from Gauss-Hermite polynomial fits to the  $H\beta$  line profile. Figure 1 shows the host-subtracted luminosity and line widths measured from the 370 narrow-line subtracted SE spectra of NGC 5548; the left panels show these observables as a function of time, and the right panels show corresponding distributions, with the mean and dispersions listed. The dispersions in these quantities are non-random and due primarily to the intrinsic variability of the AGN but also include small random measurement uncertainties.

### 2.3.2. Reverberation Virial Masses

To effect the most meaningful comparison with the single-epoch masses, we calculate reverberation-based virial products,  $M_{\text{vir}}$ , for each data set. Using radii from reverberation mapping leads to masses that are independent of the uncertainties introduced in obtaining SE radii measurements (i.e., AGN variability and calibration uncertainties in the  $R - L$  scaling relationship). We use the reverberation radii of Peterson et al. (2004) that are derived from the rest-frame lag,  $\tau_{\text{cent}}$ , the centroid of the cross-correlation function.

We characterize the BLR velocity dispersion by both FWHM and  $\sigma_{\text{blue}}$  of the broad  $H\beta$  emission line. Line widths are measured in the mean spectrum for each observing season of NGC 5548 (years 1–13) created from the sample of SE spectra used in each analysis and the full PG1229 data set after removal of the narrow-line components. We use the same methods and line boundaries as were used for the SE spectra. Here, we measure line widths in the mean spectrum (Collin et al. 2006) rather than the rms spectrum (Peterson et al. 2004) because there is no analog for the rms spectrum for a SE spectrum. Instead, by using the mean spectrum, we are still measuring the approximate mean BLR velocity dispersion<sup>3</sup> yet retain a comparable line profile to a single-epoch spectrum to use for a direct comparison. Uncertainties in these line width measurements are determined with the bootstrap method of Peterson et al. (2004). We then combine the reverberation radii for each year of the NGC 5548 sample and the single radius for PG1229 with the corresponding values of each

---

<sup>3</sup>The main justification for using the rms spectrum is that only the portions of the line profile varying in response to the ionizing continuum contribute to the rms spectrum. See Collin et al. (2006) for a discussion.

line width measurement to calculate two sets of RM virial products for each data set: one using FWHM and one using  $\sigma_{\text{blue}}$ . Weighted mean virial products are then calculated for the NGC 5548 data sets spanning multiple years: 1 – 10 for the variability, constant component, and  $S/N$  analyses in §§3.1 – 3.3 and 6 – 13 for the blending analysis in §3.4, providing two final reverberation virial masses for each data set: one using  $\sigma_{\text{blue}}$  and one using FWHM.

### 2.3.3. Comparisons: Measuring Precision and Accuracy

We measure the precision of SE virial masses by creating distributions of the SE virial masses calculated for each data set as described above. The dispersion,  $\sigma_{\text{SE}}$ , of these distributions serves as a measure of the precision of the SE masses. It gives an indication of how well multiple SE spectra can reproduce a single, mean mass,  $\langle \log M_{\text{SE}} \rangle$ . In addition, the accuracy of the SE masses can be gauged by measuring the systematic offset of this mean mass from the corresponding reverberation virial mass determined for a given data set. We define this offset as  $\langle \Delta \log M \rangle = \langle \log M_{\text{SE}} \rangle - \log M_{\text{vir}}$  and calculate a value for each SE mass distribution.

## 2.4. Evaluation of Constant Components

A copy of each flux calibrated spectrum was made, and the narrow emission lines were removed from this copy to allow for the calculation and comparison of virial products from spectra with and without narrow lines present. Narrow  $\text{H}\beta$   $\lambda 4861$  and the  $[\text{O III}]$   $\lambda\lambda 4959, 5007$  lines were removed by first creating a template narrow line from the  $[\text{O III}]$   $\lambda 5007$  line in the mean spectrum from each data set. This template was then scaled in flux to match and remove the  $[\text{O III}]$   $\lambda 4959$  line and narrow component of  $\text{H}\beta$  (Peterson et al. 2004).

Host galaxy starlight contributions to the flux were determined for the various extraction apertures of all NGC 5548 and PG1229 spectra using the method of Bentz et al. (2008) and observations of both galaxies with the High Resolution Channel of the Advanced Camera for Surveys on the *Hubble Space Telescope*. Luminosities (and subsequently SE virial masses) were calculated for every spectrum with and without the presence of this constant continuum component.

## 2.5. Spectral Decomposition: Deblending the Spectral Features

The rather simple approach used above to measure line widths and to account for host galaxy contamination using local continuum fitting techniques fails to address certain spectral features or components that may systematically affect our SE virial mass estimates. First, the global AGN continuum is power-law shaped, rather than linear, as we fit above. This may lead to small uncertainties in our continuum subtraction, possibly even over the small wavelength range used here. Second, blended Fe II emission exists throughout the optical spectrum. If strong, this emission could complicate our definitions of local continua on either side of the H $\beta$ , [O III]  $\lambda\lambda$ 4959, 5007 region, potentially adding flux both to these continuum regions and to H $\beta$  itself. Third, the red wing of broad He II  $\lambda$ 4686 emission may be blended with the blue wing of H $\beta$ . This could also contaminate the local continuum region defined between these two lines as well as the line width measurement. Fourth, the underlying galaxy spectrum has structure that may be imprinted on the broad line profiles if not removed accurately.

Therefore, we undertake full spectral decompositions of a selection of NGC 5548 spectra. Our goal is to determine if the (potentially over-) simplified local continuum-fitting prescription to account for the underlying host galaxy and additional AGN emission skew the SE virial mass results in a significant, yet correctable manner. The data set used in this section consists of the 33 Shane Telescope spectra from the AGN Watch sample described above. Because spectral decomposition gives model-dependent, non-unique solutions, we compare results based on two independent methods utilizing multi-component fits to account for contributions from the host galaxy, AGN continuum, and spectral emission lines.

### 2.5.1. Method A

Decomposition method A (e.g., Wills et al. 1985) assumes that the observed spectra can be described as a superposition of five components (see Dietrich et al. 2002, 2005, for more details):

1. An AGN power law continuum ( $F_\nu \sim \nu^\alpha$ ).
2. A host galaxy spectrum (Kinney et al. 1996).
3. A pseudo-continuum due to merging Fe II emission blends.
4. Balmer continuum emission (Grandi 1982).

5. An emission spectrum of individual emission lines, such as  $H\alpha$ ,  $[\text{N II}]\lambda\lambda 6548, 6583$ ,  $\text{He I } \lambda 5876$ ,  $H\beta$ ,  $[\text{O III}]\lambda\lambda 4959, 5007$ ,  $\text{He II } \lambda 4686$ .

The first four components are simultaneously fit to each single-epoch spectrum, minimizing the  $\chi^2$  of the fit. We tested several different host galaxy templates (elliptical galaxies, S0, and spiral Sa and Sb galaxies). The best results were obtained using a scaled spectrum of the E0 galaxy NGC 1407, which is quite appropriate for the bulge of NGC 5548. From this template we measure an average host starlight contribution of  $F_{\text{gal}}(5100 \text{ \AA}) = (4.16 \pm 0.84) \times 10^{-15} \text{ erg s}^{-1} \text{ cm}^{-2} \text{ \AA}^{-1}$  for this sample. This is highly consistent with the value of  $F_{\text{gal}}(5100 \text{ \AA}) = (4.45 \pm 0.37) \times 10^{-15} \text{ erg s}^{-1} \text{ cm}^{-2} \text{ \AA}^{-1}$  derived with the Bentz et al. (2008) procedure for the observed aperture of ( $4'' \times 10''$ ) for this data. To account for the Fe II emission, we use the rest-frame optical template covering 4250 – 7000  $\text{\AA}$  based on observations of I Zw 1 by Boroson & Green (1992). The width of the Fe II emission template was on average  $\text{FWHM} = 1160 \pm 34 \text{ km s}^{-1}$ . For the Balmer continuum emission, we found that the best fit was obtained for  $T_e = 15,000 \text{ K}$ ,  $n_e = 10^8 \text{ cm}^{-3}$ , and optically thick conditions.

The best fits of these components, including the power-law fit to account for AGN continuum emission, are subtracted from each spectrum, leaving the AGN emission-line spectrum intact. Narrow emission-line components were then subtracted by creating a template narrow line from a two-component Gaussian fit to the  $[\text{O III}]\lambda 5007$  narrow line and then scaling it to each individual narrow line to be subtracted based on standard emission line ratios. Figure 2 illustrates the different fit components and residuals for a typical spectrum of NGC 5548. Overall, the spectrum is quite well reconstructed. However, it can be seen that around  $\lambda \simeq 5200 \text{ \AA}$  to  $\lambda \simeq 5800 \text{ \AA}$  the flux level is overestimated. This might indicate that it is necessary to include an additional component due to Paschen continuum emission, as suggested by Grandi (1982) and more recently by Korista & Goad (2001). This may, in turn, result in the selection of a less red host galaxy spectrum but potentially a better overall fit (Vestergaard et al. 2008). This component was not included here, however, because the actual strength of the Paschen continuum emission is not yet well constrained and will therefore be the topic of future work in this area.

### 2.5.2. Method B

This method first corrects the spectra for Galactic reddening using the extinction maps of Schlegel et al. (1998) and the reddening curve of O’Donnell (1994) with  $E(B - V) = 0.0392$ . The continuum and emission lines were modeled separately. The continuum components include the following:

1. A nuclear power-law continuum.
2. The Fe II and Fe III blends that form a “pseudo-continuum” across much of the UV-optical range. Template modeling is the only way, at present, to provide a reasonable iron emission model for subtraction (see, e.g., Vestergaard & Wilkes 2001; Véron-Cetty et al. 2004, and references therein). We used the optical iron template of Véron-Cetty et al. (2004), varying only the strength of the template and the line widths.
3. The Balmer continuum was modeled using the prescription of Grandi (1982) and Dietrich et al. (2002), with an adopted electron temperature of 10,000 K and an optical depth at the Balmer edge of 1.0. These Balmer continuum parameters typically give good matches to quasar spectra (Vestergaard et al. 2008). We note that here, too, no attempt was made to model the Paschen continuum as it is poorly constrained.
4. The underlying host-galaxy spectrum was modeled using the stellar population model templates of Bruzual & Charlot (2003). The best-fit model was a single elliptical galaxy template with stellar ages of 10 Gyr. This model seems to slightly underestimate the stellar emission strength in NGC 5548 longward of H $\alpha$  (e.g.,  $\gtrsim 7000\text{\AA}$ ), but preliminary fits (not included) seem to indicate the overall fit is better with the inclusion of the Paschen continuum.

The individual continuum model components were varied to provide the optimum match to the observed spectrum using Levenberg-Marquardt least-squares fitting and optimization. Based on the host galaxy template fits for this decomposition method, we measure a host starlight contribution of  $F_{\text{gal}}(5100\text{\AA}) = (7.05 \pm 1.28) \times 10^{-15} \text{ erg s}^{-1} \text{ cm}^{-2} \text{\AA}^{-1}$ , larger than found by Bentz et al. (2008) and the method A value, but marginally consistent once these other values take Galactic reddening into account. The best fit continuum components were then subtracted from the spectrum, and the remaining emission-line spectrum was modeled with Gaussian functions using the same optimization routine as for the continuum. A single Gaussian profile, whose width was allowed to vary up to  $600 \text{ km s}^{-1}$  was used for each of the narrow emission lines, but the same width was used for all narrow lines. The strength of the [O III]  $\lambda\lambda 4959, 5007$  doublet lines was constrained to the 1:3 ratio set by atomic physics. Figure 3 shows the individual and combined components fit to the same NGC 5548 spectrum as in Figure 2, as well as the residual spectrum after subtraction of both continuum components and the narrow emission lines.

### 2.5.3. Methodical Differences and Mass Calculations

Overall, the two methods for fitting the individual AGN spectral components agree quite well. However, there are two differences worth noting. First, each method uses a different optical Fe II emission line template. The Fe II template used by method B (Véron-Cetty et al. 2004) includes narrow line region contributions to the emission. In general, both templates are similar, but they differ in detail at around  $\lambda \simeq 5000 \text{ \AA}$  and  $\lambda \gtrsim 6400 \text{ \AA}$ . However, the strength of the optical Fe II emission in NGC 5548 is quite weak (Vestergaard & Peterson 2005), and the width of the Fe II emission is expected to be broad. Therefore, the choice of the Fe II emission template has little impact on the results in this case. Second, the modeling of the narrow emission lines in the  $H\beta$  and [O III]  $\lambda\lambda 4959, 5007$  region with the single Gaussian component of method B sometimes leaves some residuals around the [O III]  $\lambda\lambda 4959, 5007$  lines. This typically happens when excess emission appears in the red wing of  $H\beta$  which cannot be fully accounted for with only Gaussian components. Although these residuals do not account for a significant amount of flux, the two-component Gaussian fit to the narrow lines used by method A tends to better minimize these residuals.

Line widths are measured for  $H\beta$  from all epochs following analysis from both spectral decomposition methods as well as the local continuum fitting method. For this particular sample, the local continuum was defined between two continuum windows over the rest-frame wavelength ranges  $4730 - 4745 \text{ \AA}$  and  $5090 - 5110 \text{ \AA}$ , and line widths were measured in all spectra over the rest-frame wavelength range  $4747 - 4931 \text{ \AA}$ , as determined from the mean spectrum. For the local continuum-fitted spectra,  $L_{5100}$  was calculated from the average continuum flux density over the rest-frame wavelength range  $5090 - 5110 \text{ \AA}$  after correcting for host galaxy starlight. For decomposition methods A and B,  $L_{5100}$  was taken to be the value of the power-law fit to each SE spectrum at rest-frame  $5100 \text{ \AA}$ . SE virial masses were then calculated with equation 2 for line widths measured with both  $\sigma_{\text{blue}}$  and FWHM.

For comparison to the SE mass distributions of each of the three data analysis methods, reverberation virial masses were calculated with each of the line width measures, FWHM and  $\sigma_{\text{blue}}$ , similar to the previous NGC 5548 data sets spanning multiple years. The weighted mean RM virial mass for each analysis method (covering yrs 6–11 and 13 for this data set) was calculated by averaging the yearly RM virial masses calculated by combining line widths measured from the mean spectrum created from SE spectra spanning a single observing season and the BLR radius from the corresponding season as determined with reverberation mapping (for results from individual years, see Peterson et al. 2004).

### 3. Analysis and Results

#### 3.1. Effects of Variability

To investigate systematics associated strictly with AGN variability in SE virial products (VPs), we first remove the contaminating constant spectral components (i.e., narrow lines and host galaxy flux) as described in §2.4. Figure 4 shows virial mass distributions created from all 370 spectra of NGC 5548 (Fig. 4a) and 32 spectra of PG1229 (Fig. 4b). Results are shown for both line width measures,  $\sigma_{\text{blue}}$  and FWHM (left and right panels, respectively), for both objects. For each distribution we focus on the dispersion (i.e., precision) and the mean offset (i.e., accuracy),  $\langle\Delta\log M\rangle$ , from the reverberation result, as given in Table 1. Column 1 gives the object name, column 2 shows the sample size, column 3 lists the reverberation virial product and associated uncertainties when calculated with  $\sigma_{\text{blue}}$ , column 4 lists the mean and standard deviation of the distribution utilizing  $\sigma_{\text{blue}}$ , column 5 gives the mean offset between the reverberation VP (Col. 3) and mean of the SE distribution (Col. 4). Columns 6, 7, and 8 are similar to columns 3, 4, and 5, but for masses based on FWHM.

Figure 4 shows that the widths of all four distributions are quite small. The listed dispersions have not been corrected for measurement uncertainties in line width and luminosity. However, we have estimated the average measurement uncertainties for the full set of NGC 5548 SE spectra to be 0.08 dex in  $\log(L)$ , 0.01 dex in  $\log(\sigma_{\text{blue}})$ , and 0.03 dex in  $\log(\text{FWHM})$ . We can assume that these measurement errors are independent of the dispersion due to variability alone and that the distributions are close enough to Gaussian that we can add independent errors in quadrature. Therefore, we can correct the observed dispersions in the SE mass distributions for NGC 5548 for the contribution due to these measurement uncertainties. Following this correction, the uncorrected dispersions listed in Figure 4a and Table 1 can be reduced to 0.11 dex for masses based on  $\sigma_{\text{blue}}$  and 0.14 dex for masses based on FWHM. The narrowness of these distributions indicates that the scatter in SE masses due to intrinsic variability is remarkably small. This is particularly true for PG1229, for which  $\sigma_{\text{SE}} \approx 0.05$  dex. Granted, PG1229 is less variable, but with a scatter of only 0.11 – 0.14 dex, the uncertainty in  $M_{\text{SE}}$  due to variability for NGC 5548 is not large either.

The precision and accuracy in the  $M_{\text{SE}}$  measurements seem only weakly dependent on whether  $\sigma_{\text{blue}}$  or FWHM is used as the line-width measure. For both AGNs, the scatter is apparently minimized and the accuracy (given by  $\langle\Delta\log M\rangle$ ) maximized with the use of  $\sigma_{\text{blue}}$ . In terms of accuracy,  $\langle\Delta\log M\rangle$  should at least partially represent the displacement of the particular AGN from the  $R - L$  relation, regardless of which quantity is used to characterize the line width. Figure 5 shows that the average luminosities of the NGC 5548 and PG1229 SE spectra place them above the  $R - L$  relation in  $r$  by  $\sim 0.13$  dex and  $\sim 0.07$  dex, respectively,

after accounting for host starlight contributions (as was done here). This explains why, for a given SE luminosity, the resulting radius (and thus VP) is underestimated compared to the reverberation results, confirmed by the negative  $\langle \Delta \log M \rangle$  values found in Table 1. Since this effect depends on luminosity alone, the masses calculated from both line width measures should be affected equally. However, masses calculated from FWHM measurements result in larger  $\langle \Delta \log M \rangle$  values for both objects. This additional component may be related to the fact that our measurement uncertainties tend to be larger for FWHM compared to  $\sigma_{\text{blue}}$ , or it may simply demonstrate one of the limitations of measuring masses from SE spectra with FWHM.

The light curves of NGC 5548 span several years, much longer than the reverberation time scale of tens of days. Indeed, the  $H\beta$  lag has been measured year-to-year for over a dozen different years, and the lag and the mean luminosity of the AGN are well-correlated on yearly timescales, and as noted earlier, the reverberation-based mass is approximately constant with perhaps a weak dependence on luminosity (Bentz et al. 2007). Given our goal of comparing SE predictions with reverberation measurements, we have for NGC 5548 also computed the difference between each SE virial product and the reverberation virial product for the specific year in which the SE observation was made. We show the distribution of these differences in Figure 6, which is rather narrower than the similar distribution shown in Figure 4a. This illustrates that masses from SE spectra seem to reproduce the reverberation mass that would be measured at the same time quite accurately, to  $\sim 25\%$  or so. However, there are longer term secular changes that occur, as shown in the top panel of Figure 1, that add to the observed dispersion due to variability resulting in the total width of the distributions shown in Figure 4. Because of these secular changes, even a reverberation-based mass measurement might change slightly, say, over a dynamical time scale.

### 3.2. Accounting for Constant Components

Failing to account for the constant spectral components in the AGN spectrum (i.e., the narrow emission lines and host galaxy starlight) affects both the precision and accuracy of the SE mass estimates. We examine the effect of neglecting each of these components individually and then in combination for both NGC 5548 and PG1229.



### 3.2.1. Effect of Starlight

First, we examine the consequence of failing to remove the host starlight contribution to the continuum flux density. We still subtract narrow emission-line components, however. Figure 7 shows SE virial mass distributions similar to those in Figure 4, but here the host starlight was not subtracted from the luminosity before the SE masses were calculated. In terms of precision, the virial mass distributions in Figure 7 derived from non-host-corrected luminosities have equal or even slightly smaller dispersions than their corrected counterparts (Fig. 4). This occurs simply because subtraction of the host starlight increases the relative amplitude of the AGN continuum variations. NGC 5548 has a relatively larger host galaxy contribution and is therefore more susceptible to this effect than PG1229. The observable result is an overall increase in the dispersion of the mass distribution and, in particular, the low-mass (i.e., low-luminosity state) wings of the  $M_{SE}$  distributions in Figure 7 are broadened compared to those in Figure 4. Notably, over-subtracting the host galaxy flux could also lead to similar observable consequences. However, the tail of the distribution appears to be nearly Gaussian, which argues against any large error in the starlight flux estimate. In contrast, this broadening affect is not observed for PG1229. This is expected because PG1229 has a smaller host contribution to its total luminosity than NGC 5548, and its luminosity varied less over the time period in which it was observed. Therefore, when we subtract a relatively smaller constant host flux from a distribution of values with an initially smaller luminosity dispersion, the effect on the SE mass distributions is less significant.

Failing to account for host starlight imposes a shift to the entire SE mass distribution. Because the luminosity is larger when the host contribution is not subtracted, a larger BLR radius is estimated with the  $R - L$  relation. This, in turn, produces larger virial products and affects the accuracy of the measurements. Whereas Figure 4 shows an average underestimation of the SE masses compared to the reverberation results, Figure 7 shows that on average, the SE masses are overestimated (i.e. positive  $\langle \Delta \log M \rangle$  values), which is again explained by the locations of NGC 5548 and PG1229 on the  $R - L$  scaling relationship (Fig. 5). Without accounting for the host starlight, both objects lie below the relation. Therefore, the  $R - L$  relation overestimates the radius of a SE luminosity measurement that does not account for this contribution. This effect can be seen by comparing the  $\langle \Delta \log M \rangle$  values in rows 2 and 5 of Table 2 with those of Table 1, which are negative for in Table 1 but positive in Table 2<sup>4</sup>. Failing to account for the host contribution has roughly the same overall effect on the precision and accuracy of SE mass distributions regardless of whether  $\sigma_{\text{blue}}$  or FWHM

---

<sup>4</sup>Results in Table 2 are presented in a similar manner as Table 1, except columns have been added to distinguish whether or not narrow emission-line and/or host starlight contributions are present in the results.

is used for the calculation of  $M_{\text{SE}}$  (a shift in  $\langle\Delta\log M\rangle$  of 0.17 dex for NGC 5548 and 0.12 dex for PG1229 for both line width measures), as expected since this contribution does not affect the line width.

Based on the results presented here, it is not completely clear that subtracting the host contribution improves the overall accuracy of the mass estimates. In fact, the SE masses of both NGC 5548 and PG1229 presented here are typically as accurate or more accurate (i.e., the absolute value of  $\langle\Delta\log M\rangle$  is smaller) when the starlight contribution is not subtracted. When considering the physics of AGNs, however, the BLR radius should be correlated with only the AGN luminosity, since the material in the BLR knows nothing of the luminosity originating from galactic starlight. Furthermore, Bentz et al. (2008) determine that calibrating the  $R - L$  relation with luminosity measurements that have been corrected for host starlight contamination significantly reduces the scatter in the relationship and results in a slope that is highly consistent with that predicted by simple photoionization theory. These considerations, in addition to our use of the Bentz et al. (2008) host starlight-corrected calibration of the  $R - L$  relation for SE mass determinations, serve as motivation for removing this contamination before the  $R - L$  relation is used. This evidence suggests that the ambiguity between the theoretical expectation that host-subtracted luminosities should yield more accurate masses and the fact that the masses presented here are more accurate before host starlight subtraction is simply because both NGC 5548 and PG1229 happen to lie above the  $R - L$  relation. However, in a general statistical sense, SE masses will be overestimated if host starlight contamination is not taken into account before the  $R - L$  relation is used to determine BLR radii. This is particularly true for lower-luminosity, Seyfert-type galaxies that, in contrast to quasars, have larger relative host starlight contributions to their measured luminosity.

### 3.2.2. *Effect of Narrow Lines*

The  $H\beta$  and  $[\text{O III}]\lambda\lambda 4959, 5007$  emission line profiles for NGC 5548 and PG1229 are shown in Figure 8. In NGC 5548 (left), the narrow line typically increases the peak flux by  $\sim 50\%$ , compared to  $\lesssim 10\%$  in PG1229 (right). Given these relative contributions of narrow-line fluxes (particularly in the case of NGC 5548), failing to subtract the narrow line component from the broad emission line before measuring the width can have a significant impact on the resulting mass estimate. To demonstrate this, Figure 9 displays SE mass distributions for NGC 5548 and PG1229; this time, however, we do not subtract the narrow lines from the spectra before measuring line widths, although we do subtract the host galaxy contribution. Statistics for the scenarios shown in Figure 9 can be found in Table 2, rows 3

and 6. Figure 9 clearly demonstrates that leaving the narrow lines present affects both the precision and accuracy of the SE masses.

Failing to subtract the narrow lines tends to decrease the precision of the SE mass estimates. This is evident by an increase in the width of the SE mass distributions and is particularly pronounced for NGC 5548 when characterizing the line with FWHM (by comparing Fig. 9a with Fig. 4a or Fig. 7a, in which narrow lines were removed). In this case (Fig. 9a, right), the resulting width of the VP distribution is a factor of three to four larger than if  $\sigma_{\text{blue}}$  is used (Fig. 9a, left). This effect of the narrow lines on the precision is less apparent in PG1229 because the narrow line constitutes only a small percentage of the  $H\beta$  line flux. However, it is still observed when the FWHM is used for measuring the line widths (compare Fig. 9b, left, to Fig. 4b, left), since, to reiterate, this trend is much more apparent for the FWHM.

From a physical standpoint, only BLR emission varies in response to the ionizing continuum on reverberation timescales, so only the broad emission component should be used for the virial mass calculation. Because the square of the line width enters into the BH mass calculation, relatively small changes in the line width can significantly affect the mass estimate. When the narrow-line component is not subtracted, the line width and hence the black hole mass is underestimated. Figure 9 shows evidence for this in both NGC 5548 and PG1229. As with the precision, this effect is much stronger when the narrow component is a more prominent feature in the emission-line profile, as is the case for NGC 5548 (refer back to Fig. 8). For obvious reasons, removing the narrow lines is more important when the line width is measured with the FWHM (right panels of Figs. 9a and 9b); the very definition of the FWHM depends on the peak flux, so if the narrow component is not subtracted, this peak flux can be greatly overestimated. An overestimation of the peak flux results in an artificially small FWHM and, subsequently, a severely underestimated mass. NGC 5548 affords a useful case in point: the masses calculated without removing narrow line components (Figure 9a) are underestimated on average by a whole order of magnitude ( $\langle\Delta\log M\rangle = -1.00$ ) when line widths are measured from the FWHM (right panel). In contrast, the dependence of the line dispersion on the line center and peak flux is relatively weak, affecting the accuracy of SE mass estimates by  $\sim 0.1 - 0.2$  dex for NGC 5548 and by an insignificant amount for PG1229 (compare  $\langle\Delta\log M\rangle$  values for  $M_{\text{SE}} \propto \sigma_{\text{blue}}$  from Table 2, Rows 3 and 6 to Table 1 values). Regardless of the minimal effect when  $\sigma_{\text{blue}}$  is used, the evidence presented here clearly indicates that the narrow line component should be removed regardless of which prescription is used for measuring the line width.

### 3.2.3. Combined Effects of Starlight and Narrow Lines

Figure 10 shows mass distributions for both NGC 5548 and PG1229 when neither of these constant components is removed from the spectra. Table 2 (Rows 1 and 4) displays the corresponding statistics. Generally, as expected, the precision and accuracy are worse, or at least no better than when these constant components are removed. However, these two constant components act opposingly on the mass: failing to remove the narrow lines tends to decrease mass estimates, but failing to subtract host galaxy flux increases mass estimates. Therefore, these two effects can fortuitously cancel, resulting in an apparently smaller dispersion and/or mean offset. This is the case for PG1229 when FWHM is used to measure the line width and NGC 5548 when  $\sigma_{\text{blue}}$  is used. The chance cancellation in these cases should not distract from the otherwise well-supported conclusion that both of these components should be removed to obtain the most accurate and precise SE mass estimates.

## 3.3. Systematic Effects due to $S/N$

Our goal here is to identify the point at which low  $S/N$  begins to compromise the precision and accuracy of SE mass determinations. We start with our most homogeneous data set, the 270 observations of NGC 5548 from the Perkins Telescope. Based on conclusions from previous sections §§3.1 and 3.2, only narrow-line-subtracted spectra that have been corrected for host galaxy starlight are used. The  $S/N$  per pixel of the original spectra ranges significantly, with a mean and standard deviation of  $110 \pm 50$ , as measured across the  $5100\text{\AA}$  continuum window given above. Using the  $S/N$  per pixel in the original spectra as a starting point, we then increase the noise in each spectrum by applying a random Gaussian deviate to the flux of each pixel across the whole spectrum. The magnitude of the deviate is set to achieve degraded  $S/N$  levels of  $\sim 20$ ,  $\sim 10$ , and  $\sim 5$  across the  $5100\text{\AA}$  continuum window. Figure 11 shows an example degradation for a typical NGC 5548 spectrum. Below, we discuss results for masses calculated from line widths measured directly from the data as well as from Gauss-Hermite fits to  $H\beta$  in the original and  $S/N$  degraded spectra.

### 3.3.1. Direct Measurement of the Spectra

We measure line widths and luminosities directly from both the original and  $S/N$ -degraded spectra and calculate virial masses. The resulting distributions are shown in Figure 12 for both  $\sigma_{\text{blue}}$  (left) and FWHM (right). Statistics describing the distributions of  $M_{\text{SE}}$  are listed in Table 3 in a format similar to that of previous tables. Figure 12 shows that

the dispersions of the distributions broaden as the  $S/N$  of the spectra decreases. Overall, low  $S/N$  begins to negatively affect the precision of the virial mass estimates at  $S/N \lesssim 10$  for  $\sigma_{\text{blue}}$  (see third panel on left) and at  $S/N \lesssim 5$  for FWHM (see bottom panel on right). Wilhite et al. (2007) find a similar result, with the widths of their SE mass distributions increasing steadily with decreasing  $S/N$ . However, measurements of  $\sigma_{\text{blue}}$  and FWHM are affected differently by decreasing  $S/N$  and will therefore be discussed separately.

Measurements of virial masses from  $\sigma_{\text{blue}}$  in low  $S/N$  spectra sacrifices both precision and accuracy primarily because the wings of the broad line become lost in the noise and the line profile boundaries cannot be accurately defined for cases where  $S/N \lesssim 10$ . This results in smaller effective line widths. This effect decreases the overall accuracy by shifting the whole distribution to artificially smaller masses. However, at these low  $S/N$  limits (see bottom two plots of Fig. 12, left), the distribution actually becomes highly non-Gaussian in shape, resulting in a much peakier distribution, nearly centered on the corresponding reverberation virial product. This implies that although the overall dispersion has increased significantly (by nearly a factor of 2) and individual measurements have the potential to be highly inaccurate, a typical measurement will likely be more accurate with a much smaller uncertainty than quoted through the overall distribution average.

Different systematics are introduced when using FWHM to characterize the line width. Because FWHM does not depend on the line wings, lower  $S/N$  can be tolerated before the precision is significantly sacrificed. When  $S/N$  is low enough to affect FWHM, the line width is generally underestimated. Several effects contribute to the difficulty in defining FWHM in low  $S/N$  data. First, the peak flux may be incorrectly attributed to the highest noise spike, resulting in an overestimated maximum. Second, the half-maximum may be difficult to define because the continuum level cannot be accurately ascertained. Third, the width may also be problematic to define because a noisy profile could mean that the half-maximum flux value is shared by multiple wavelength values. These effects alter the precision at our lowest degraded  $S/N$  level ( $\sim 5$ ). However, they begin to affect the accuracy of the measurement much earlier. Progressively poorer accuracy can be easily observed from the increasingly negative  $\langle \Delta \log M \rangle$  values in the distribution statistics given in Table 3 for FWHM and/or by comparing the mean values of the distributions in Figure 12, right. Although higher precision VP measurements can be made from lower  $S/N$  data with the FWHM than with  $\sigma_{\text{blue}}$ , there is a trade-off in accuracy. For this reason, we caution against measuring SE masses from spectra with  $S/N$  lower than  $\sim 20 \text{ pixel}^{-1}$ , regardless of the line-width measurement method.

### 3.3.2. Measurements from Gauss-Hermite Polynomial Fits

Recent work has been published in which the emission line profiles are fit with either Gaussian and/or Lorentzian profiles (e.g., McLure & Dunlop 2004; Shen et al. 2008a,b) or Gauss-Hermite polynomials (e.g., Woo et al. 2007; McGill et al. 2008). SE virial masses are then calculated with the line widths measured from these fits rather than directly from the data in an attempt to mitigate the negative effects of low  $S/N$  on line-width determinations. We test this technique by fitting a sixth-order Gauss-Hermite polynomial to the narrow-line-subtracted  $H\beta$  profiles in the original and  $S/N$ -degraded spectra used above. A linearly interpolated continuum defined by the same regions as above was first subtracted from the spectra before the fits were made. Our Gauss-Hermite polynomials utilize the normalization of van der Marel & Franx (1993) and the functional forms of e.g. Cappellari et al. (2002). We then use the method of least-squares to determine the best coefficients for the sixth-order polynomial fit. The thick black curves in Figure 11 show an example of the fits to the original and  $S/N$ -degraded forms of this typical NGC 5548 spectrum. Both FWHM and  $\sigma_{\text{blue}}$  were measured from these fits with the same methods described previously for the direct measurements and then combined with host-corrected luminosities in order to calculate virial masses for all SE spectra in this sample. Figure 13 shows the resulting distributions for the virial masses calculated using  $\sigma_{\text{blue}}$  (left) and FWHM (right). Distribution statistics are also given in Table 3.

We can now compare the mass distributions from the fitted data to our previous results (Fig. 12; Table 3) based on direct measurement. We find that low  $S/N$  is somewhat mitigated by using  $\sigma_{\text{blue}}$  to characterize the line width of fits to the data (Fig 13, left). The fits allow increased precision at the  $S/N \sim 10$  level, compared to measurements directly from the spectra. In addition, the accuracy of the VPs resulting from the fits is also nearly unchanged down to  $S/N \sim 10$ . Although the fits routinely underestimate the line peak, this does not greatly affect the  $\sigma_{\text{blue}}$  results because of the insensitivity of this line characterization to the line center. Therefore, Gauss-Hermite fits are advantageous for extending the usefulness of data down to  $S/N \sim 10$  if  $\sigma_{\text{blue}}$  is used to characterize the line width.

On the other hand, our fit results do not show an improvement if FWHM is used for the line widths, at least as far as this object is concerned. The Gauss-Hermite fits were often unable to accurately model the complex  $H\beta$  profile of NGC 5548, and the underestimation of the line peak by the fits that was mentioned previously causes a systematic overestimation of FWHM that increases with decreasing  $S/N$ . This overestimation of FWHM acts in the opposite direction as the trend observed with the direct FWHM measurements from the data (i.e. a typical underestimation of FWHM). Therefore, as the  $S/N$  decreases, a significantly increasing difference results between the mean value of the  $M_{\text{SE}}$  distributions

based on direct measurement and those based on the Gauss-Hermite fits. From a precision standpoint, the width of the  $M_{\text{SE}}$  distribution based on Gauss-Hermite fits to the original  $S/N$ -level spectra is actually narrower than that of the equivalent distribution resulting from direct measurement. This suggests that fitting the line profile when using FWHM may actually be beneficial in high  $S/N$  data and reduce possible systematics such as residuals from narrow-line subtraction. However, once the  $S/N$  is degraded, the dispersions of the distributions composed of masses calculated from the fits (Fig. 13, right) quickly become larger than those composed of masses calculated from direct measurement (Fig. 12, right). This shows that fitting the line profile when using FWHM does not mitigate the effects of low  $S/N$  because the fit does not accurately reproduce the true profile shape.

For the sake of completeness, we note that there are many different methods described in the literature for measuring FWHM that are formulated to address issues associated with noisy data and complex line profiles. Here, we have chosen two methods (the formulation of Peterson et al. (2004) and the use Gauss-Hermite polynomial fits) that differ in computational complexity and the assumptions made about the underlying profile shape. However, other methods also attempt to mitigate the effects of noise. For example, Brotherton et al. (1994) define the peak of the line based on a flux weighted mean wavelength, the centroid, above a level that is 85% of the line peak to decrease the likelihood that the peak used is simply a noise spike. Similarly, Heckman et al. (1981); Busko & Steiner (1989) also calculate the centroid with  $\gtrsim 80\%$  of the peak flux but use it in a slightly different way to determine the line width. Results using any of these other methods are not expected to differ greatly from the results that we show here, however, since our two methods effectively represent the extremes for measuring this naively simple quantity.

### 3.4. Systematic Effects Due to Blending

As noted earlier, the best subset of NGC 5548 spectra to use to explore the effects of blending of spectral features is the 33 spectra from the Lick Observatory 3m Shane Telescope. These are high  $S/N$ , homogeneous spectra that have the broad spectral coverage necessary for spectral decomposition. Since spectral decomposition does not necessarily lead to a unique solution, two independent methods were employed as described earlier. Cumulative distribution functions created from the SE masses measured from the 33 Lick Observatory spectra of NGC 5548 are shown in Figure 14. Distributions of  $M_{\text{SE}}$  are presented for all three data analysis methods described above: the local continuum fitting method (left panels), spectral decomposition method A (center panels), and spectral decomposition method B (right panels). As in previous plots, mass results are shown for both  $\sigma_{\text{blue}}$  (Fig. 14a) and

FWHM (Fig. 14b). Table 4 displays the corresponding statistics for the distributions shown in Figure 14.

When  $\sigma_{\text{blue}}$  is used in the VP calculation, a full spectral decomposition gains a small amount of precision relative to the simple, local continuum fitting method. More importantly though is that a systematic offset is seen between the mean values of the local continuum-fitted distribution versus those of decomposition methods A and B. Line dispersions measured from the deblended spectra (for both methods A and B) are consistently larger than those measured using a local continuum fit. This is demonstrated in Figure 15, where we have plotted the  $\sigma_{\text{blue}}$  measurements from the spectra deblended with methods A and B against those based on a local continuum fit. This difference is due to a combination of two factors<sup>5</sup>. First, the host galaxy templates used for both decomposition methods contain a small  $\text{H}\beta$  absorption feature that effectively adds additional flux to the center of the  $\text{H}\beta$  emission line when the host is subtracted. This absorption is not accounted for by a linear continuum fit. However, since  $\sigma_{\text{blue}}$  is only weakly dependent on the line peak, this is unlikely to make a significant contribution to the observed difference. The second and larger contributing factor to the differences in  $\sigma_{\text{blue}}$  measurements is a result of blending of  $\text{H}\beta$  with  $\text{He II } \lambda 4686$ . Decarli et al. (2008) have suggested that this blending with  $\text{He II } \lambda 4686$  complicates the measurement of the line dispersion for  $\text{H}\beta$  widths larger than  $2500 \text{ km s}^{-1}$ . However, we observe larger differences for narrower  $\text{H}\beta$  widths, and therefore deduce that this blending is a stronger function of the flux of  $\text{He II } \lambda 4686$  rather than the width of  $\text{H}\beta$ . The effects of blending are therefore greater when the AGN is in a higher luminosity state, when  $\text{He II } \lambda 4686$  is stronger, even though the  $\text{H}\beta$  line is narrower in high states. This is supported by the trend seen in Figure 15 of larger  $\sigma_{\text{blue}}$  differences for narrower  $\text{H}\beta$  widths.

The blending of  $\text{He II } \lambda 4686$  and  $\text{H}\beta$  could cause an overestimation of the continuum flux level in the local continuum window defined between these lines (see §2.5.3). An overestimated continuum level leads to a steeper linear fit, a subsequent over-subtraction of the blue wing region of  $\text{H}\beta$ , and finally, an underestimation of  $\sigma_{\text{blue}}$ . The power-law continuum fit used for the decomposition methods is not susceptible to this, since it is not fit based on local continuum regions. On the other hand, the  $\sigma_{\text{blue}}$  measurements from the decompositions could be overestimated if some of the flux attributed to  $\text{H}\beta$  is actually from the red wing of  $\text{He II } \lambda 4686$ . Figure 16 shows a comparison of the continuum-subtracted mean spectrum

---

<sup>5</sup>A third factor that could also lead to differing line dispersion measurements is the presence of  $\text{Fe II}$  emission. Strong  $\text{Fe II}$  emission can obscure the line wings and line boundaries as well as contaminate the true AGN continuum level, leading to smaller line dispersion measurements. Fortunately,  $\text{Fe II}$  emission is very weak in NGC 5548, and therefore does not contribute to the differences observed here. However, this may not be the case for other objects.



formed from all SE spectra from each of the three data analysis methods. It is clear that more flux exists in the blue wing of the deblended spectra from both methods A and B than in the spectrum formed by subtracting the local continuum fit. This is a consequence of the way the continuum was fit in each case in connection with the presence of He II  $\lambda 4686$ .

Because of the large differences we observe in  $\sigma_{\text{blue}}$  measurements between the decomposition methods and the local continuum fitting method, we return to each of our decomposition methods and fit additional contributions to account for helium emission. Starting with the deblended spectra we previously created with decomposition method A, we first remove the H $\beta$  profile by modeling the emission with a scaled template created from a four-component Gaussian fit (two components for the main emission and two to account for broader wings) to H $\alpha$ , whose blue wing is unobstructed by broad emission-line blending. The template is fixed in velocity space and then scaled in flux to minimize the residuals of the fit. For these 33 spectra, the best fits result in Balmer decrements typically in the range of 2.8 – 3.2. The H $\beta$  fit is then subtracted from the spectrum, leaving the He II  $\lambda 4686$  emission line clearly visible. This emission is then fit with either a single broad Gaussian profile or a double Gaussian profile (adding a narrower component in addition to the broad component fits 19 out of the 33 epochs better than a single component, possibly due to residual narrow-line emission). The best fit profile for each epoch is subtracted from the initial, narrow-line subtracted, deblended spectrum. Figure 17 (top) shows the H $\beta$  region of the mean spectrum formed from the SE spectra after spectral decomposition with method A before and after subtracting the mean He II  $\lambda 4686$  fit, which is also shown. This method fits He II  $\lambda 4686$  only as a means to better understand the blending with H $\beta$ .

In contrast, with method B, we return to the continuum-subtracted spectra (i.e. after removing contributions from the host starlight, Balmer continuum, power-law continuum, and FeII emission) and simultaneously fit both broad and narrow optical emission lines. Similar to the method described above for the continuum component fitting, method B uses Levenberg-Marquardt least-squares fitting and optimization to obtain the best overall emission-line fits to the full spectrum. In addition to fitting the narrow-line features as described above, the three strongest broad Balmer lines are each fit with two Gaussian profiles, where the best fit velocity width is held fixed for all three lines. Both He II and He I emission lines are fit with a single Gaussian profile, and although these widths are not tied to the Balmer line widths, the widths of He II  $\lambda 4686$  and the He I emission under the H $\beta$ , [O III]  $\lambda\lambda 4959, 5007$  region are tied to the width of the unblended He I  $\lambda 5876$  line in the same way the Balmer line widths are tied together. Each set of emission lines of a given species and type of emission (i.e. narrow or broad) is isolated in the total fit, so that only the emission of interest can be subtracted. Since the narrow-line emission was subtracted previously, we now subtract the broad helium emission, effectively deblending H $\beta$  from He II  $\lambda 4686$ . Figure

17 (bottom) shows the  $H\beta$  region of the mean spectrum created from the 33 SE spectra after decomposition with method B before and after subtracting the average helium fit, which is also shown.

We measure line widths in these He-deblended spectra with a newly-defined blue boundary for  $H\beta$  at  $4720\text{\AA}$  (compared to  $4747\text{\AA}$  previously). This boundary was extended because the edge of the blue wing of  $H\beta$  is better discerned without the presence of  $\text{He II } \lambda 4686$ . Figure 18 shows new  $\sigma_{\text{blue}}$  measurements for the He-deblended  $H\beta$  line from the two decomposition methods compared again to  $\sigma_{\text{blue}}$  from the local continuum method. The  $\sigma_{\text{blue}}$  measurements from method A still disagree with the local continuum fitting method as much as, if not more than, before subtraction of  $\text{He II } \lambda 4686$ . However, the new  $\sigma_{\text{blue}}$  measurements from method B are now consistent with the local continuum fitting method.

The observed differences in these new  $\sigma_{\text{blue}}$  measurements between method A and method B come from the procedure and assumptions that each method uses to fit the spectral emission lines. The line widths from method B now agree with the local continuum fitting method because the combined best fit to both lines tends to result in an  $H\beta$  profile that basically sits on top of a broad  $\text{He II } \lambda 4686$  profile. In the wavelength region between the two emission lines (i.e. where the local continuum is defined), the difference between the continuum level and the flux level observed in the blended spectrum is usually attributed completely to  $\text{He II } \lambda 4686$  emission by method B. Therefore, when  $\text{He II } \lambda 4686$  is subtracted, the flux level of this region is reduced nearly to the level of the continuum, which is what is assumed by the local continuum fitting method, thus making these two methods consistent. On the other hand, method A subtracts the  $H\beta$  with an  $H\alpha$  template before fitting  $\text{He II } \lambda 4686$ . Because the  $H\alpha$  profile has very extended wings, this method necessarily assumes that  $H\beta$  also has this extended, broad component. Therefore, nearly opposite to method B, method A effectively fits a  $\text{He II } \lambda 4686$  profile that is sitting on top of a very broad  $H\beta$  profile and consequently subtracts a smaller  $\text{He II } \lambda 4686$  component. This results in  $\sigma_{\text{blue}}$  measurements that are equally or even more inconsistent with previous measurements because it extends the  $H\beta$  wing under the  $\text{He II } \lambda 4686$  profile. Because this extended blue wing is hidden under  $\text{He II } \lambda 4686$ , method A results suggest that the local continuum fitting method is significantly underestimating  $\sigma_{\text{blue}}$  (by as much as 40%).

Evidence suggests that the helium lines are consistently broader than the Balmer lines in Type 1 AGNs (Osterbrock & Shuder 1982). This is always the case in the rms spectrum of AGNs that have been monitored for reverberation mapping studies, as well. Additionally, in the few cases for which reverberation lags could be measured for  $\text{He II } \lambda 4686$  the lags are shorter than the corresponding  $H\beta$  lag in the same object (see Peterson et al. 2004). This suggests that given the virial hypothesis for a single source, the material responsible for

He II  $\lambda 4686$  emission is closer to the central source than that responsible for the H $\beta$  emission and moving at a faster velocity, thus producing broader emission lines. Method B supports this evidence with the emission line models and results described above. On the other hand, although the fits of method A do not reproduce the same broad He II  $\lambda 4686$  emission, the assumption this method makes about the similarities that should exist between the shape of the H $\alpha$  and H $\beta$  profiles are hard to discount, given that these two species should exist in similar regions of the BLR. Instead, our analysis demonstrates that there is not a unique method to account for the blending of H $\beta$  and He II  $\lambda 4686$  that results in consistent line dispersion measurements of H $\beta$ . Therefore, we conclude that this blending is a potential problem for the use of  $\sigma_{\text{blue}}$  in calculating  $M_{\text{SE}}$ .

Blending is less likely to be a limitation for reverberation mapping studies that use the line dispersion measured in the rms spectrum, however. Blending between H $\beta$  and He II  $\lambda 4686$  is often lessened in the rms spectrum because the broad wings of the lines that are the most blended tend not to be as variable as the more central parts of the line. To test this, we characterized the H $\beta$  line width with  $\sigma_{\text{blue}}$  in the 3 rms spectra formed from the three sets of spectra created during the deblending analysis (after the local continuum fit, decomposition method A, and decomposition method B). We did not account for He II  $\lambda 4686$  emission in the rms spectrum before measuring  $\sigma_{\text{blue}}$  in the local continuum subtracted rms spectrum. However, the He II  $\lambda 4686$  emission in the two rms spectra formed after decomposition methods A and B was modeled with a single Gaussian profile and subtracted. We find that measurements of  $\sigma_{\text{blue}}$  from the rms spectra from all three methods are consistent to within  $1\sigma$ . This consistency suggests that the masses determined through reverberation studies that use the line dispersion measured from the rms spectrum are not as susceptible as SE masses to this bias in  $\sigma_{\text{blue}}$  caused by blending. Additionally, it is worth noting that not all AGNs have strong blending of He II  $\lambda 4686$  and H $\beta$ , superceding the need for such caution with the use of  $\sigma_{\text{blue}}$ .

Different concerns arise when FWHM is used to characterize the H $\beta$  line width. Figure 14b demonstrates that all three methods are in agreement, on average, with equally good precision and moderately small offsets from their respective reverberation results (given in Table 4). The small systematic difference between the mean SE masses of the decomposition methods and the local continuum fit is most likely due to the small H $\beta$  absorption feature present in the host galaxy light, as discussed above. Figure 19 shows that FWHM, unlike the line dispersion, is less sensitive to the details of measurement, however. The differences seen in the line dispersion measurements are not present for the FWHM measurements, since blending in the wings and the definition of the continuum have a much smaller effect on the FWHM value. However, these general observations and the FWHM statistics in Table 4 exclude the outliers at the low-mass end of the distributions in Figure 14b, shown by the

thin black curves (also labeled in Fig. 19). These points are outliers because of a particularly complex line profile, characterized by an asymmetric red bump, present in these two epochs (JD2452030 and JD2452045). These epochs illustrate that FWHM can be complicated by profile features such as the gross asymmetries and double peaks that the broad Balmer lines sometimes exhibit.

Figure 20 shows how FWHM is defined for the  $H\beta$  profile on JD2452030 for each of the two decomposition methods and for a local continuum fit. In each case, we measure FWHM following the procedure of Peterson et al. (2004). The differences in the FWHM measurements for this spectrum are due in part to the complex profile of this line and in part to the differences in the peak flux of the line for the different methods. Figure 20 shows that each of the three methods removes slightly different amounts of narrow-line emission. These small differences change the total flux in the line by at most a few percent, but the change in the line peak combined with the complex profile are sufficient to cause large differences in the measurements of FWHM, and thus  $M_{\text{SE}}$ .

Despite the observed differences in the SE  $\sigma_{\text{blue}}$  measurements between each decomposition method after accounting for He II  $\lambda 4686$  blending, masses derived from both methods otherwise differ very little. The dispersions in the SE mass distributions from both methods are nearly equal, however masses derived with the use of method A seem somewhat more accurate, with smaller  $\langle \Delta \log M \rangle$  values than method B.

#### 4. Discussion and Conclusion

We have undertaken a careful examination of some of the systematics associated with measurements of emission-line widths for the purpose of calculating black hole virial masses from single-epoch spectra. The systematics on which we focused our attention are (i) intrinsic AGN variability, (ii) contributions by constant spectral components, (iii)  $S/N$  of the data, and (iv) blending with the different spectral components, particularly the underlying host galaxy.

Throughout this analysis we have not displayed a preference for either the line dispersion or the FWHM to characterize the line width and have instead shown that there are both advantages and limitations to each measure. Specifically, FWHM provides consistent results for lower  $S/N$  spectra without the use of profile fits, and it is much more robust in the presence of blending. However, FWHM should only be used in spectra that have had the narrow line components carefully removed, as the sensitivity of FWHM to the presence and/or removal method of narrow emission lines is a serious limitation. On the other hand,

the line dispersion is advantageous in this respect, since it is rather insensitive to the details of narrow-line component subtraction. However, its use should be limited to data characterized by relatively high  $S/N$  or with profile fits to the emission lines. Unlike FWHM, the greatest limitation of using the line dispersion is blending in the line wings, and use of the line dispersion should therefore be avoided if there is emission line blending that has not been modeled and removed. As we have shown here, however, even in the case of modeling, the accuracy of the model may be questionable. In the case of NGC 5548, if decomposition model B is correct (i.e., where the He II  $\lambda 4686$  line is fit assuming the same velocity width as the unblended He I  $\lambda 5876$  line), then correcting for the blending of H $\beta$  and He II  $\lambda 4686$  by modeling and subtracting the helium emission produces consistent results with the local continuum-fitting method. However, if method A is the more accurate representation of the blending (i.e., where the He II  $\lambda 4686$  line was modeled assuming the line profile of H $\beta$  is the same as H $\alpha$ ), then there will be a resulting mean offset in the SE masses of  $\sim 0.1$  dex compared to the local continuum-fitting method due to underestimation of the blended H $\beta$  line dispersion in the latter method. Because of these difficulties, when blending complicates the line profile shape or boundaries of SE spectra, it is best to use FWHM.

To summarize the effects of these systematics on SE masses, Table 5 gives an error budget displaying how each systematic affects the uncertainties in SE mass estimates in terms of increasing or decreasing the precision and accuracy of the measurement, where we generalize our results here to both low luminosity Seyfert-type AGNs and quasars. While nearly all of the systematic uncertainties we investigated add to the dispersion in the SE mass distributions in varying amounts, some effects also cause often severe systematic shifts in the distributions, leading to overall under- or overestimations of SE masses. Readers should be particularly cautious about these effects because large statistical studies cannot average out these types of systematics. In summarizing the sources of error covered here, we use the same description of the precision and accuracy as above, with the accuracy described as an offset in the mean SE virial mass, and the precision described by the dispersion in the mass distribution. In Table 5, however, we assume that errors are independent and the distributions are close enough to Gaussian that we can add independent errors in quadrature to determine the cumulative effect. We therefore describe the additional offset and dispersion due to each systematic with respect to the SE mass calculation which results in the minimum observed uncertainties (i.e., Fig. 4). In Table 5 we consider the following individual sources of error in the SE masses for both characterizations of the line width:

1. Random measurement errors. These are simply due to inherent uncertainties in any measurement of luminosity and line width. Empirically, we determine these uncertainties by comparing measurements of closely spaced observations, assuming that these parameters change little over very short time scales (i.e., time scales much shorter

than the reverberation time scale). We use this empirical method to estimate the uncertainties for the line width and luminosity of the NGC 5548 data set, which we propagate through to determine uncertainties in the mass estimates, listed in Table 5. Uncertainties are not listed for quasars because the size of the PG1229 data set is much smaller and with fewer closely spaced observations than that of NGC 5548. We could therefore not accurately estimate uncertainties in this manner. However, given the small observed dispersion in the SE virial masses for PG1229 ( $\sim 0.05$  dex), measurement uncertainties are likely to be very small.

2. Variability on reverberation timescales (see Fig. 6 and Fig. 4b). Our analysis on reverberation-timescale variability shows that SE spectra can reproduce the reverberation-based virial product that would be measured at the same time to about 0.10 dex (i.e.,  $\sim 25\%$ ) for Seyferts and to about 0.05 dex (i.e.,  $\sim 15\%$ ) for quasars. This is an interesting result, given the quadrature sum of the individual dispersions in luminosity and line width for NGC 5548 add to be  $\sim 0.17$  dex, regardless of line width measure. This is significantly larger than the dispersion in the virial masses, and therefore confirms the presence of a virial relation between the line width and luminosity (i.e., the BLR radius). An additional ramification for quasars is that the dispersion for PG1229 determined here represents more than a factor of two less than even the formal, observational uncertainties in the reverberation mass for this object. This suggests that once the zero point and slope of scaling relations such as the  $R - L$  relation are accurately determined, it may be more accurate to simply use the scaling relations to determine masses of individual sources than to make direct mass measurements. It also follows that SE mass estimates can then easily be acquired with relative certainty for high redshift objects, as long as the extrapolation of the scaling relations to these luminosity regimes is valid.
3. Longer-term secular variations. At least in the case of NGC 5548, we see that longer-term (dynamical timescale?) variations cause changes in both the SE and reverberation-based virial product. The amplitude of these variations is similar to those on reverberation time scales, creating an additional dispersion in the SE virial products of about 0.09 or 0.05 dex for FWHM and  $\sigma_{\text{blue}}$ , respectively. This longer-term secular variability adds to the reverberation-scale variability described above (and seen in Figure 6) to produce the observed dispersion (Fig. 4a) in the SE virial product for Seyferts. We cannot estimate the contribution of secular variations to the observed dispersion for quasars, since all the data available for PG1229 was used in a single reverberation experiment and observations did not span dynamical timescales for this object.

4. Combined minimum uncertainty. The combination of the above effects sets a “minimum observable uncertainty” for SE-based masses, given in line 4 of Table 5 (see also Fig. 4). Adding measurement uncertainties, reverberation timescale variability, and longer-term secular variability effects in quadrature yields an estimate of the observable dispersion in SE masses for Seyferts of  $0.12 - 0.16$  dex ( $\sim 30 - 45\%$ ) and less for quasars (although the long-term secular effects are unexplored in this case).
5. Failure to remove host galaxy starlight. Host galaxy contamination causes an overestimation of the luminosity and thus the mass. The effect of this contamination on the precision of SE mass estimates is minimal so it does not further broaden the distribution of mass measurements. Instead, it affects the accuracy of the mass estimate, resulting in an additional mean offset, listed in Table 5, compared to the offset observed when the host contamination is removed (Also compare the mean distribution values of Figs. 4 and 7). The size of the systematic overestimation of the mass depends on the fraction of host starlight contamination, however. Since both NGC 5548 and PG1229 lie near the middle of the sample of AGNs used to set the slope of the  $R - L$  relation, the effect due to host-galaxy contamination could be much worse or more minimal depending on whether the luminosity is much smaller or larger (respectively) than the objects presented here (Bentz et al. 2008).
6. Failure to remove narrow  $H\beta$ . The  $H\beta$  narrow emission-line component is by far the biggest source of error for both Seyferts and quasars when using FWHM to characterize the line width, adding significantly to the dispersion and offset, as shown in Table 5. In particular, this offset causes SE masses to be underestimated by nearly an order of magnitude for Seyfert-type galaxies that often have strong narrow-line components. Notice, however, that because of the insensitivity of  $\sigma_{\text{blue}}$  to the line center, this effect increases the dispersion of the SE mass distributions very little or not at all when the line width is characterized by  $\sigma_{\text{blue}}$ . However, the systematic offset for the  $\sigma_{\text{blue}}$  case is still nearly doubled compared to the offset observed for the minimum uncertainty case. This makes it imperative to remove narrow line components before measuring line widths, regardless of how the line width is characterized.
7. Limitations due to  $S/N$ . Direct measurements from low  $S/N$  spectra add an additional systematic offset in the SE mass measurements because of a systematic underestimation of the line width, as well as decreased precision in these measurements. Our fits to the line profiles do increase the usefulness of  $S/N$ -level  $\sim 10$  spectra with  $\sigma_{\text{blue}}$ . However, they generally make things worse for FWHM, leading to lower precision masses than when direct measurements of the line widths are used, as well as systematic overestimations of the line width and mass, an effect that is opposite to that observed when

measuring FWHM directly from the data. Therefore, to avoid either underestimating SE masses when measuring line widths directly from the data or overestimating SE masses when line profiles are fit, SE mass studies should be conducted using high  $S/N$  ( $\gtrsim 20 \text{ pixel}^{-1}$ ) spectra.

The authors are grateful to C. A. Onken for the use of his Gauss-Hermite fitting software. We would also like to thank David Weinberg for many useful comments and suggestions which improved several aspects of this paper. This work has been supported by the NSF through grant AST-0604066 and by NASA through grant AR-10691 from the Space Telescope Science Institute, which is operated by AURA, Inc., under NASA contract NAS5-26555. This research has made use of the NASA/IPAC Extragalactic Database (NED) which is operated by the Jet Propulsion Laboratory, California Institute of Technology, under contract with the National Aeronautics and Space Administration.

## REFERENCES

- Bentz, M. C., Peterson, B. M., Pogge, R. W., Vestergaard, M., & Onken, C. A. 2006, *ApJ*, 644, 133
- Bentz, M. C., et al. 2007, *ApJ*, 662, 205
- . 2008, *ApJ*, submitted
- Blandford, R. D., & McKee, C. F. 1982, *ApJ*, 255, 419
- Boroson, T. A., & Green, R. F. 1992, *ApJS*, 80, 109
- Brotherton, M. S., Wills, B. J., Francis, P. J., & Steidel, C. C. 1994, *ApJ*, 430, 495
- Bruzual, G., & Charlot, S. 2003, *MNRAS*, 344, 1000
- Busko, I. C., & Steiner, J. E. 1989, *MNRAS*, 238, 1479
- Cappellari, M., Verolme, E. K., van der Marel, R. P., Kleijn, G. A. V., Illingworth, G. D., Franx, M., Carollo, C. M., & de Zeeuw, P. T. 2002, *ApJ*, 578, 787
- Collin, S., Kawaguchi, T., Peterson, B. M., & Vestergaard, M. 2006, *A&A*, 456, 75
- Corbett, E. A., et al. 2003, *MNRAS*, 343, 705



- Decarli, R., Labita, M., Treves, A., & Falomo, R. 2008, MNRAS, 387, 1237
- Dietrich, M., Appenzeller, I., Vestergaard, M., & Wagner, S. J. 2002, ApJ, 564, 581
- Dietrich, M., Crenshaw, D. M., & Kraemer, S. B. 2005, ApJ, 623, 700
- Elvis, M. 2000, ApJ, 545, 63
- Ferrarese, L., & Ford, H. 2005, Space Science Reviews, 116, 523
- Ferrarese, L., & Merritt, D. 2000, ApJ, 539, L9
- Ferrarese, L., Pogge, R. W., Peterson, B. M., Merritt, D., Wandel, A., & Joseph, C. L. 2001, ApJ, 555, L79
- Fine, S., et al. 2008, ArXiv e-prints, 807
- Gebhardt, K., et al. 2000a, ApJ, 539, L13
- . 2000b, ApJ, 543, L5
- Grandi, S. A. 1982, ApJ, 255, 25
- Heckman, T. M., Miley, G. K., van Breugel, W. J. M., & Butcher, H. R. 1981, ApJ, 247, 403
- Kaspi, S., Maoz, D., Netzer, H., Peterson, B. M., Vestergaard, M., & Jannuzi, B. T. 2005, ApJ, 629, 61
- Kaspi, S., Smith, P. S., Netzer, H., Maoz, D., Jannuzi, B. T., & Givon, U. 2000, ApJ, 533, 631
- Kelly, B. C., & Bechtold, J. 2007, ApJS, 168, 1
- Kinney, A. L., Calzetti, D., Bohlin, R. C., McQuade, K., Storchi-Bergmann, T., & Schmitt, H. R. 1996, ApJ, 467, 38
- Kollatschny, W. 2003, A&A, 407, 461
- Kollmeier, J. A., et al. 2006, ApJ, 648, 128
- Korista, K. T., & Goad, M. R. 2001, ApJ, 553, 695
- Kormendy, J., & Richstone, D. 1995, ARA&A, 33, 581
- Labita, M., Treves, A., Falomo, R., & Uslenghi, M. 2006, MNRAS, 373, 551

- McGill, K. L., Woo, J.-H., Treu, T., & Malkan, M. A. 2008, *ApJ*, 673, 703
- McLure, R. J., & Dunlop, J. S. 2004, *MNRAS*, 352, 1390
- Nelson, C. H., Green, R. F., Bower, G., Gebhardt, K., & Weistrop, D. 2004, *ApJ*, 615, 652
- Netzer, H. 2003, *ApJ*, 583, L5
- O'Donnell, J. E. 1994, *ApJ*, 422, 158
- Onken, C. A., Ferrarese, L., Merritt, D., Peterson, B. M., Pogge, R. W., Vestergaard, M., & Wandel, A. 2004, *ApJ*, 615, 645
- Onken, C. A., & Peterson, B. M. 2002, *ApJ*, 572, 746
- Osterbrock, D. E., & Shuder, J. M. 1982, *ApJS*, 49, 149
- Peterson, B. M. 1993, *PASP*, 105, 247
- Peterson, B. M., & Wandel, A. 1999, *ApJ*, 521, L95
- . 2000, *ApJ*, 540, L13
- Peterson, B. M., et al. 1991, *ApJ*, 368, 119
- . 1999, *ApJ*, 510, 659
- . 2002, *ApJ*, 581, 197
- . 2004, *ApJ*, 613, 682
- Schlegel, D. J., Finkbeiner, D. P., & Davis, M. 1998, *ApJ*, 500, 525
- Shen, J., Vanden Berk, D. E., Schneider, D. P., & Hall, P. B. 2008a, *AJ*, 135, 928
- Shen, Y., Greene, J. E., Strauss, M. A., Richards, G. T., & Schneider, D. P. 2008b, *ApJ*, 680, 169
- Tremaine, S., et al. 2002, *ApJ*, 574, 740
- van der Marel, R. P., & Franx, M. 1993, *ApJ*, 407, 525
- van Groningen, E., & Wanders, I. 1992, *PASP*, 104, 700
- Véron-Cetty, M.-P., Joly, M., & Véron, P. 2004, *A&A*, 417, 515
- Vestergaard, M. 2002, *ApJ*, 571, 733

—. 2004, ApJ, 601, 676

Vestergaard, M., Fan, X., Tremonti, C. A., Osmer, P. S., & Richards, G. T. 2008, ApJ, 674, L1

Vestergaard, M., & Peterson, B. M. 2005, ApJ, 625, 688

Vestergaard, M., & Wilkes, B. J. 2001, ApJS, 134, 1

Wanders, I., & Peterson, B. M. 1996, ApJ, 466, 174

Wilhite, B. C., Brunner, R. J., Schneider, D. P., & Vanden Berk, D. E. 2007, ApJ, 669, 791

Wills, B. J., Netzer, H., & Wills, D. 1985, ApJ, 288, 94

Woo, J.-H., Treu, T., Malkan, M. A., Ferry, M. A., & Misch, T. 2007, ApJ, 661, 60

Table 1. Systematic Effects due to Variability

Object	$N_{\text{SE}}$	$M (M_{\odot}) \propto \sigma_{\text{blue}}$			$M (M_{\odot}) \propto \text{FWHM}$		
		$\log M_{\text{vir}}$	$\langle \log M_{\text{SE}} \rangle \pm \sigma_{\text{SE}}$	$\langle \Delta \log M \rangle$	$\log M_{\text{vir}}$	$\langle \log M_{\text{SE}} \rangle \pm \sigma_{\text{SE}}$	$\langle \Delta \log M \rangle$
NGC 5548	370	$7.21 \pm 0.02$	$7.12 \pm 0.12$	-0.09	$8.06 \pm 0.02$	$7.95 \pm 0.16$	-0.11
PG1229+204	33	$7.28 \pm 0.25$	$7.22 \pm 0.05$	-0.06	$8.03 \pm 0.25$	$7.92 \pm 0.06$	-0.11

Table 2. Systematic Effects due to Constant Components

Object	$N_{\text{SE}}$	Narrow Lines	Host Starlight	$M (M_{\odot}) \propto \sigma_{\text{blue}}$			$M (M_{\odot}) \propto \text{FWHM}$		
				$\log M_{\text{vir}}$	$\langle \log M_{\text{SE}} \rangle$ $\pm \sigma_{\text{SE}}$	$\langle \Delta \log M \rangle$	$\log M_{\text{vir}}$	$\langle \log M_{\text{SE}} \rangle$ $\pm \sigma_{\text{SE}}$	$\langle \Delta \log M \rangle$
NGC 5548 <sup>a</sup>	370	present	present	7.21±0.02	7.21 ± 0.11	+0.00	8.06 ± 0.02	7.22 ± 0.47	−0.84
NGC 5548 <sup>b</sup>	370	removed	present	7.21±0.02	7.29 ± 0.11	+0.08	8.06 ± 0.02	8.12 ± 0.14	+0.06
NGC 5548 <sup>c</sup>	370	present	removed	7.21±0.02	7.05 ± 0.13	−0.16	8.06 ± 0.02	7.06 ± 0.52	−1.00
PG1229... <sup>a</sup>	33	present	present	7.28±0.25	7.33 ± 0.05	+0.05	8.03 ± 0.25	8.00 ± 0.07	−0.03
PG1229... <sup>b</sup>	33	removed	present	7.28±0.25	7.34 ± 0.05	+0.06	8.03 ± 0.25	8.04 ± 0.06	+0.01
PG1229... <sup>c</sup>	33	present	removed	7.28±0.25	7.21 ± 0.05	−0.07	8.03 ± 0.25	7.88 ± 0.07	−0.15

<sup>a</sup>Refer to Figure 10.

<sup>b</sup>Refer to Figure 7.

<sup>c</sup>Refer to Figure 9.

Note. — See Table 1 for the case in which both the narrow emission lines and the host starlight are removed for the virial mass calculations for both NGC 5548 and PG1229.

Table 3. Systematic Effects due to Signal-to-Noise Ratio

Data or Fit	$S/N$	$N_{SE}$	$M (M_{\odot}) \propto \sigma_{\text{blue}}$			$M (M_{\odot}) \propto \text{FWHM}$		
			$\log M_{\text{vir}}$	$\langle \log M_{SE} \rangle$ $\pm \sigma_{SE}$	$\langle \Delta \log M \rangle$	$\log M_{\text{vir}}$	$\langle \log M_{SE} \rangle$ $\pm \sigma_{SE}$	$\langle \Delta \log M \rangle$
Data	Orig	270	$7.23 \pm 0.02$	$7.12 \pm 0.14$	-0.11	$8.02 \pm 0.02$	$7.96 \pm 0.19$	-0.06
Data	$\sim 20$	270	$7.23 \pm 0.02$	$7.11 \pm 0.15$	-0.12	$8.02 \pm 0.02$	$7.93 \pm 0.18$	-0.09
Data	$\sim 10$	270	$7.23 \pm 0.02$	$7.09 \pm 0.22$	-0.14	$8.02 \pm 0.02$	$7.85 \pm 0.19$	-0.17
Data	$\sim 05$	270	$7.23 \pm 0.02$	$7.04 \pm 0.31$	-0.19	$8.02 \pm 0.02$	$7.84 \pm 0.21$	-0.18
Fit	Orig	270	$7.23 \pm 0.02$	$7.11 \pm 0.14$	-0.12	$8.02 \pm 0.02$	$8.03 \pm 0.17$	+0.01
Fit	$\sim 20$	270	$7.23 \pm 0.02$	$7.10 \pm 0.17$	-0.13	$8.02 \pm 0.02$	$8.08 \pm 0.23$	+0.06
Fit	$\sim 10$	270	$7.23 \pm 0.02$	$7.10 \pm 0.17$	-0.13	$8.02 \pm 0.02$	$8.08 \pm 0.23$	+0.06
Fit	$\sim 05$	270	$7.23 \pm 0.02$	$7.06 \pm 0.28$	-0.17	$8.02 \pm 0.02$	$8.13 \pm 0.29$	+0.11

Table 4. Systematic Effects due to Blending

Object	$N_{\text{SE}}$	Decomposition Method	$M (M_{\odot}) \propto \sigma_{\text{blue}}$			$M (M_{\odot}) \propto \text{FWHM}$		
			$\log M_{\text{vir}}$	$\langle \log M_{\text{SE}} \rangle$ $\pm \sigma_{\text{SE}}$	$\langle \Delta \log M \rangle$	$\log M_{\text{vir}}$	$\langle \log M_{\text{SE}} \rangle$ $\pm \sigma_{\text{SE}}$	$\langle \Delta \log M \rangle$
NGC 5548	33	Local Cont. Fit	$7.22 \pm 0.02$	$7.23 \pm 0.13$	+0.01	$8.16 \pm 0.02$	$8.16 \pm 0.09$	+0.00
NGC 5548	33	Method A	$7.32 \pm 0.02$	$7.31 \pm 0.10$	-0.01	$8.11 \pm 0.02$	$8.09 \pm 0.08$	-0.02
NGC 5548	33	Method B	$7.38 \pm 0.02$	$7.31 \pm 0.09$	-0.07	$8.15 \pm 0.02$	$8.08 \pm 0.09$	-0.07

Table 5. Individual Error Sources for SE Mass Measurements

Effect on $M_{\text{SE}}$	Seyfert				Quasar			
	$M \propto \text{FWHM}$		$M \propto \sigma_{\text{blue}}$		$M \propto \text{FWHM}$		$M \propto \sigma_{\text{blue}}$	
	offset	dispersion	offset	dispersion	offset	dispersion	offset	dispersion
Random measurement error:	...	0.07	...	0.04	...	... <sup>a</sup>	...	... <sup>a</sup>
Variability (RM timescales):	-0.11	0.11	-0.10	0.10	-0.11	0.06	-0.06	0.05
Longer term secular variations + slight inhomogeneity of spectra:	-0.00	0.09	+0.01	0.05	... <sup>b</sup>	... <sup>b</sup>	... <sup>b</sup>	... <sup>b</sup>
Above effects (min. uncertainty):	-0.11	0.16	-0.09	0.12	-0.11	0.06	-0.06	0.05
Additional systematics:								
Failure to remove host galaxy:	+0.17	-0.08	+0.17	-0.05	+0.12	0.00	+0.12	0.00
Failure to remove narrow H $\beta$ :	-0.89	0.49	-0.07	0.05	-0.04	0.04	-0.01	0.00
$S/N$ limitation (data, $S/N=10$ ):	-0.06	0.10	-0.05	0.18	...	...	...	...
(data, $S/N=05$ ):	-0.07	0.14	-0.10	0.29	...	...	...	...
$S/N$ limitation (fit, $S/N=20$ ):	+0.17	0.17	-0.04	0.12	...	...	...	...
(fit, $S/N=10$ ):	+0.17	0.17	-0.04	0.12	...	...	...	...
(fit, $S/N=05$ ):	+0.22	0.24	-0.08	0.25	...	...	...	...

<sup>a</sup>Uncertainties could not be determined; see Discussion, §4, individual sources of error (1).

<sup>b</sup>Uncertainties could not be determined; see Discussion, §4, individual sources of error (3).



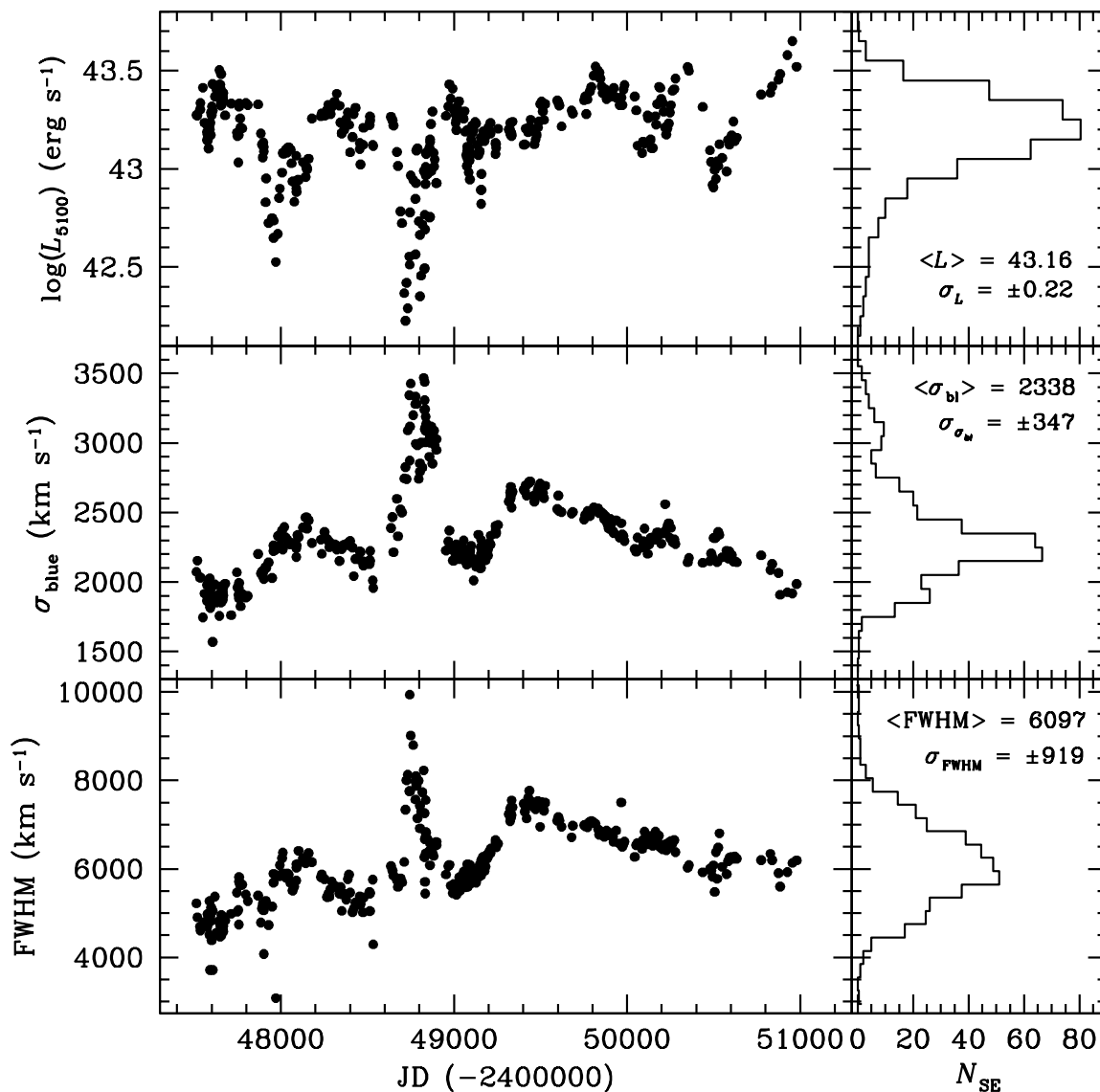


Fig. 1.— Starlight-corrected luminosity and narrow-line subtracted  $H\beta$  line width measurements from the full set of NGC 5548 spectra. Left panels show individual SE measurements as a function of time, and right panels show distributions of each measured quantity, with the mean and standard deviation of the sample given.

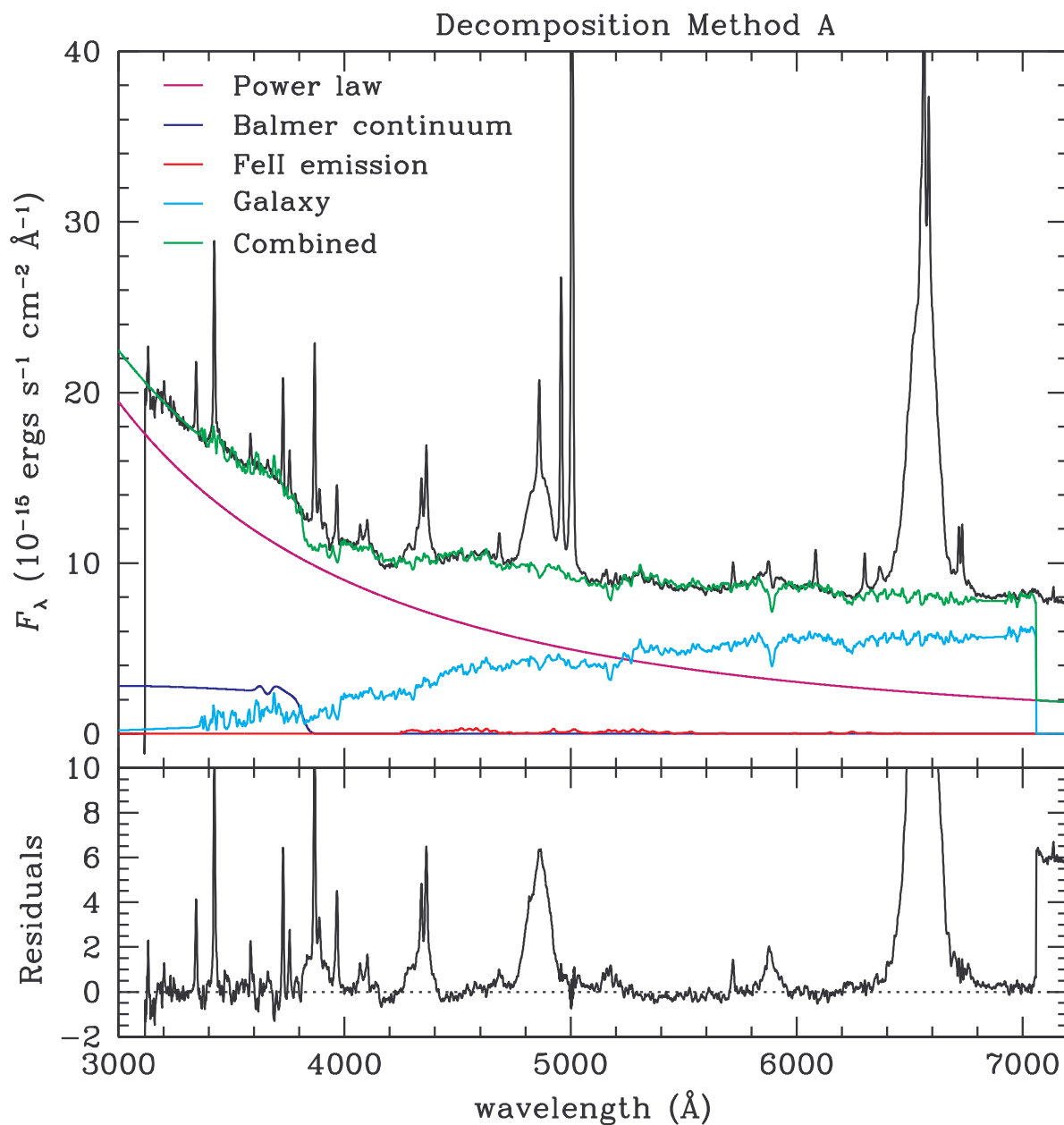


Fig. 2.— The multi-component fit to a typical spectrum of NGC 5548 for decomposition method A. In the top panel, the rest-frame spectrum shown together with a four-component fit: a power-law continuum, a host-galaxy spectrum, Balmer continuum emission, and weak optical Fe II emission. The combined fit is displayed in green. In the bottom panel, the corresponding residual spectrum is presented after additional subtraction of the narrow emission-line components (not shown).

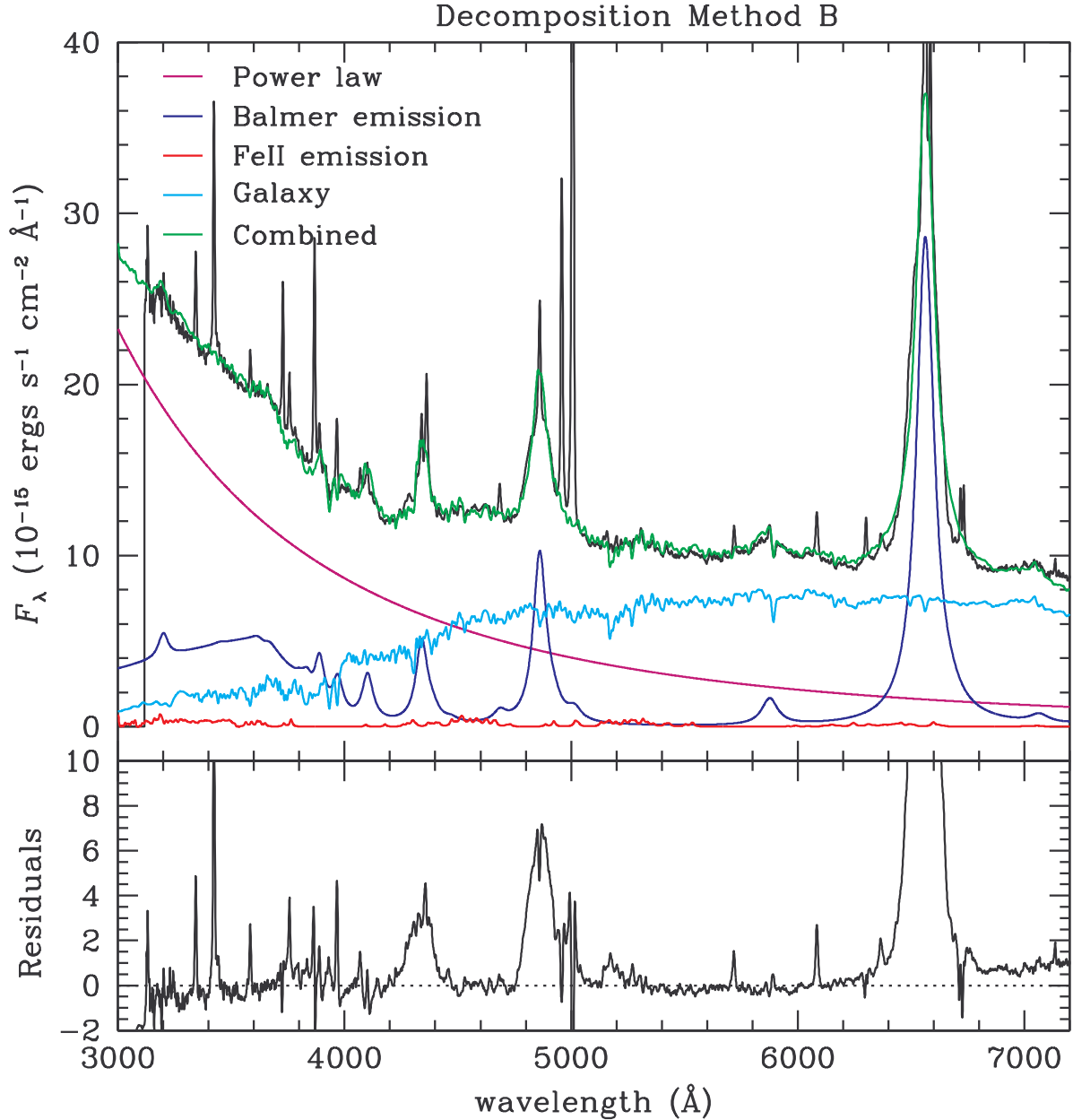


Fig. 3.— The multi-component fit to a typical spectrum of NGC 5548 for decomposition method B. In the top panel the rest frame spectrum shown has been corrected for Galactic extinction and is shown together with a four-component fit: a power-law continuum, a host-galaxy spectrum, Balmer continuum and broad-line emission, and weak optical FeII emission. The combined fit is displayed in green. Note: the Balmer line emission shown here is only included to prevent the fitting routine from attempting to assign continuum emission components to the profile wings and is not included in the final fit that is subtracted to create the residual spectrum (bottom). In addition, the residual spectrum presented also includes additional subtraction of narrow emission-line components, not shown.

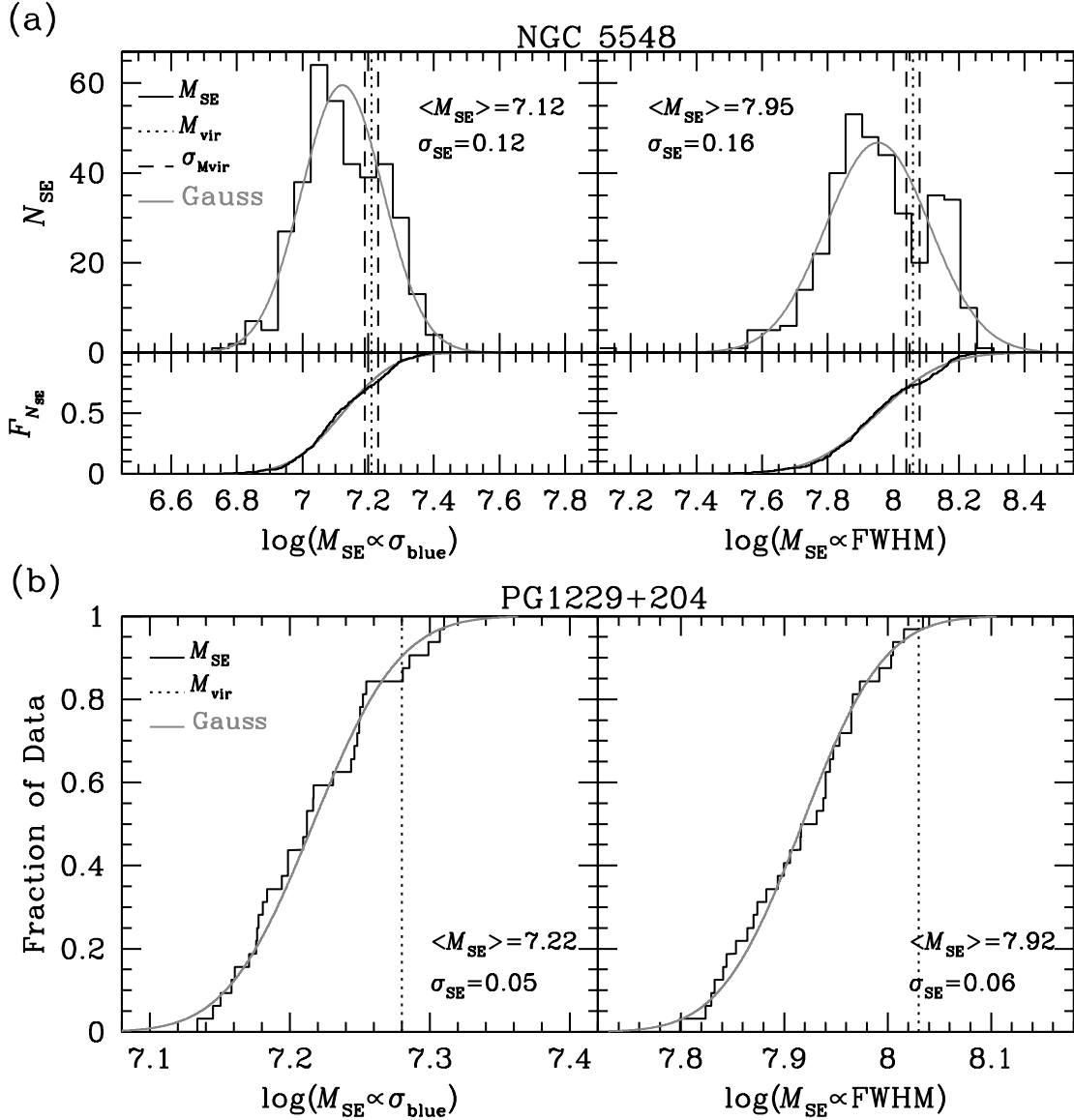


Fig. 4.— Virial mass distributions for the full NGC 5548 (a) and PG1229 (b) data sets. The Solid lines show the distributions of virial masses calculated with equation 2 using both  $\sigma_{blue}$  (left) and the FWHM (right) to measure  $H\beta$  line widths: histograms for the larger NGC 5548 data set and cumulative distribution functions (CDFs) for the smaller PG1229 data set. Narrow lines and host galaxy starlight have been subtracted from all spectra before calculating masses. A Gaussian function with the same mean, dispersion, and area as the data is overplotted in gray. The distribution mean and dispersion is shown in each plot, where values listed have not been corrected for random measurement uncertainties (see §3.1). For each data set and line width measure, the vertical lines represent the reverberation virial mass (dotted) with measurement uncertainties (dashed; not shown for PG1229 because they are typically larger than the widths of the distributions).

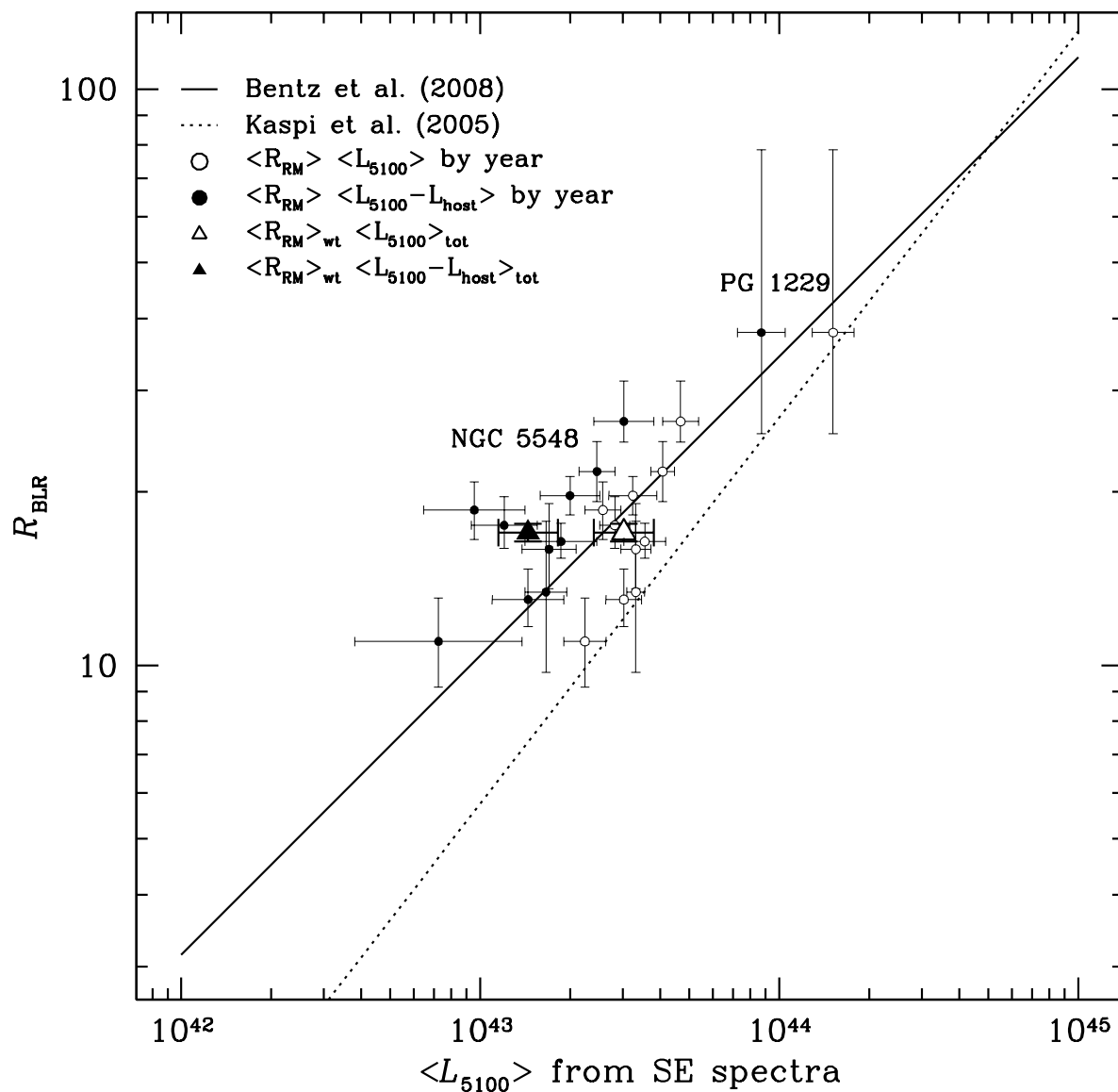


Fig. 5.— Broad line region radius-luminosity relationship for the PG1229 data and weighted mean as well as individual years of NGC 5548 data. Points are plotted for luminosities both before and after subtracting the host galaxy starlight contribution to the 5100 Å continuum flux. The Bentz et al. (2008) relation and the Kaspi et al. (2005) relation are shown for reference.

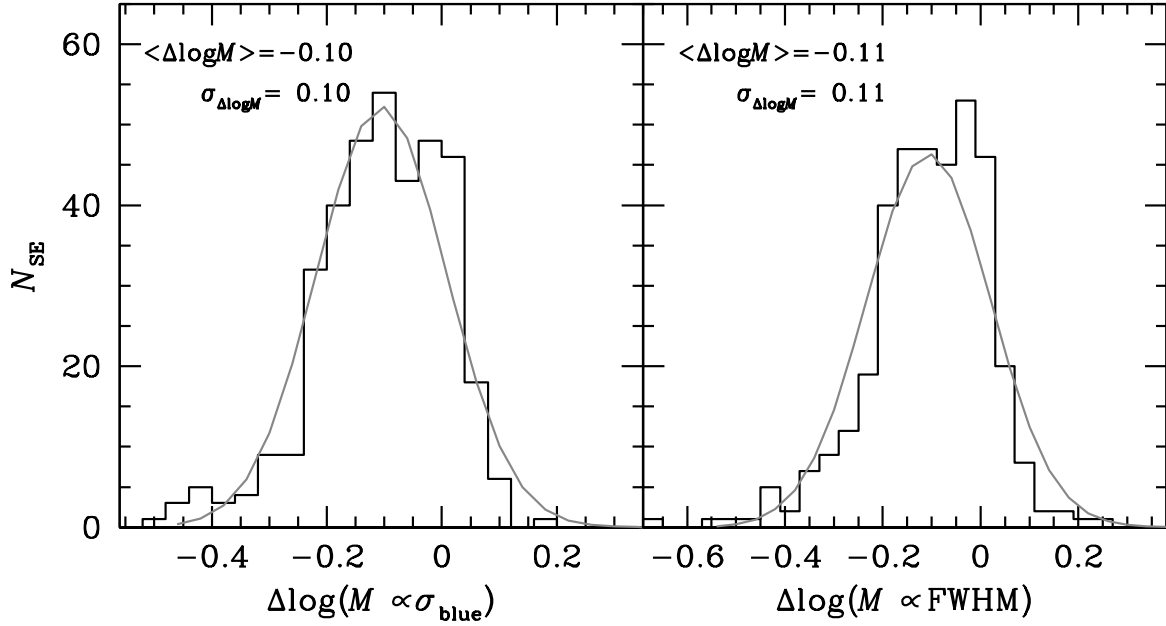


Fig. 6.— Distributions of the differences between each SE mass in a given observing year and the reverberation virial mass from that same year, plotted for masses calculated with  $\sigma_{blue}$  (left) and FWHM (right). Mass differences are shown for every spectrum in the full sample of 370 observations of NGC 5548 after subtraction of narrow emission-line components and host starlight contribution.

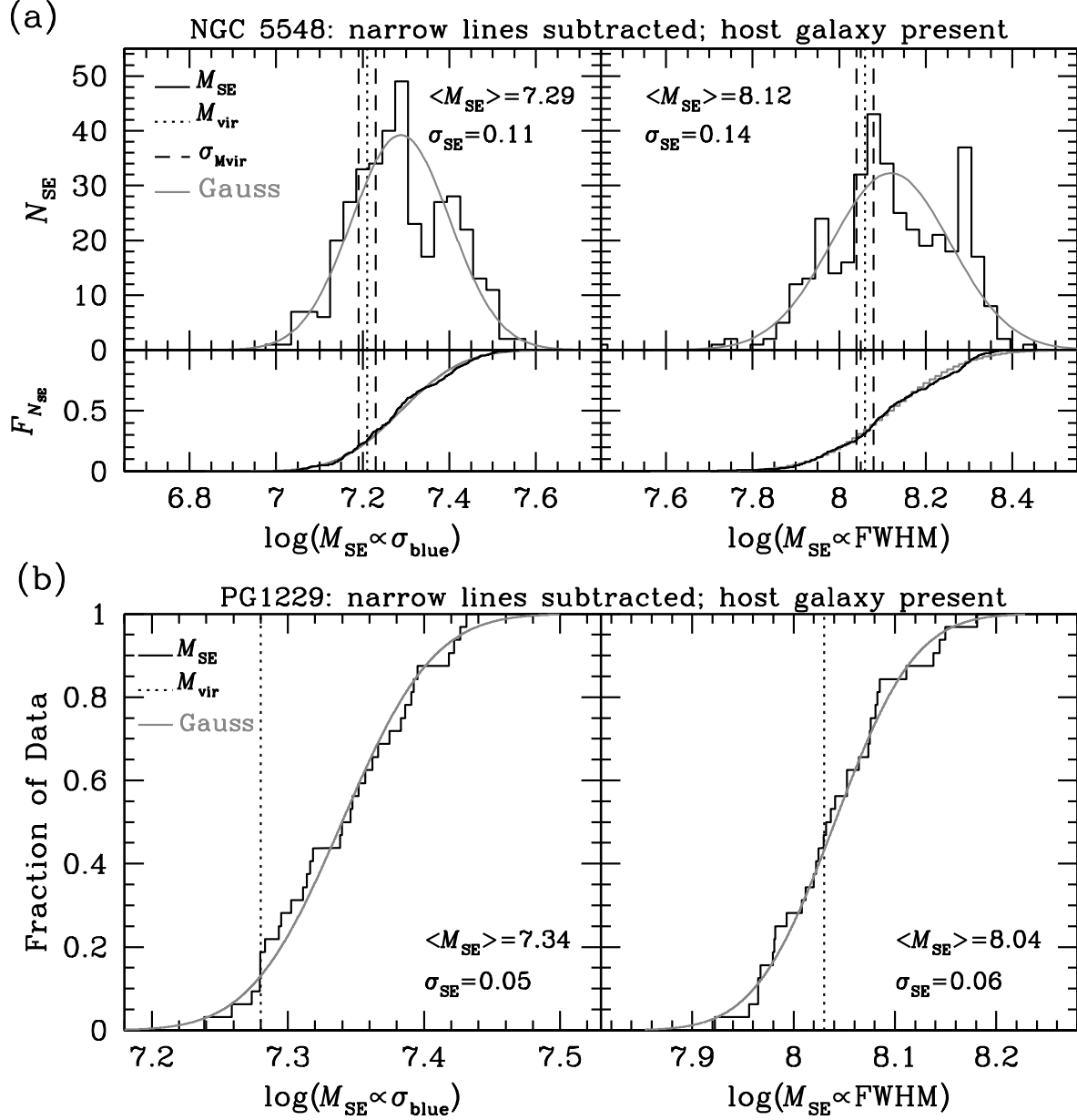


Fig. 7.— Same as Figure 4, except the host-galaxy flux contribution has not been removed. The narrow-line components have been subtracted from the spectra before measuring the  $H\beta$  line width and calculating the black hole mass.

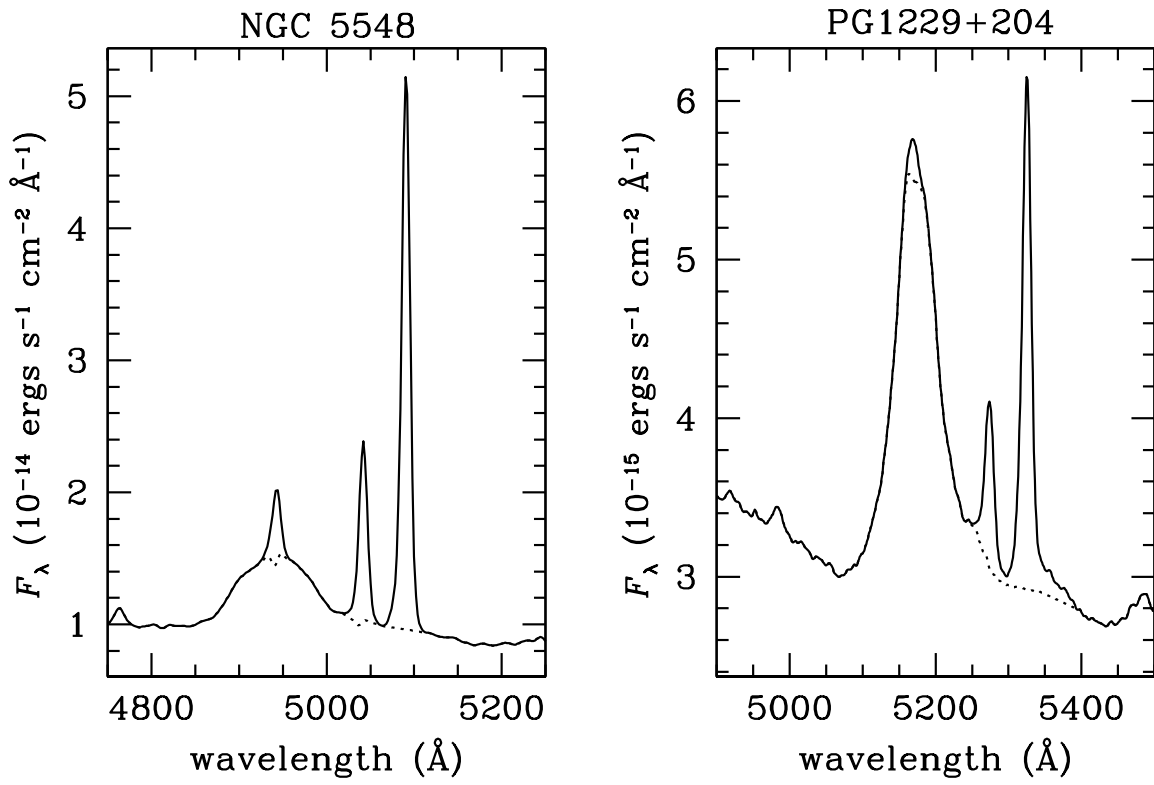


Fig. 8.— Mean spectra of NGC 5548 (left) and PG1229 (right) with narrow emission lines (solid) and after subtraction of the narrow emission lines (dotted).



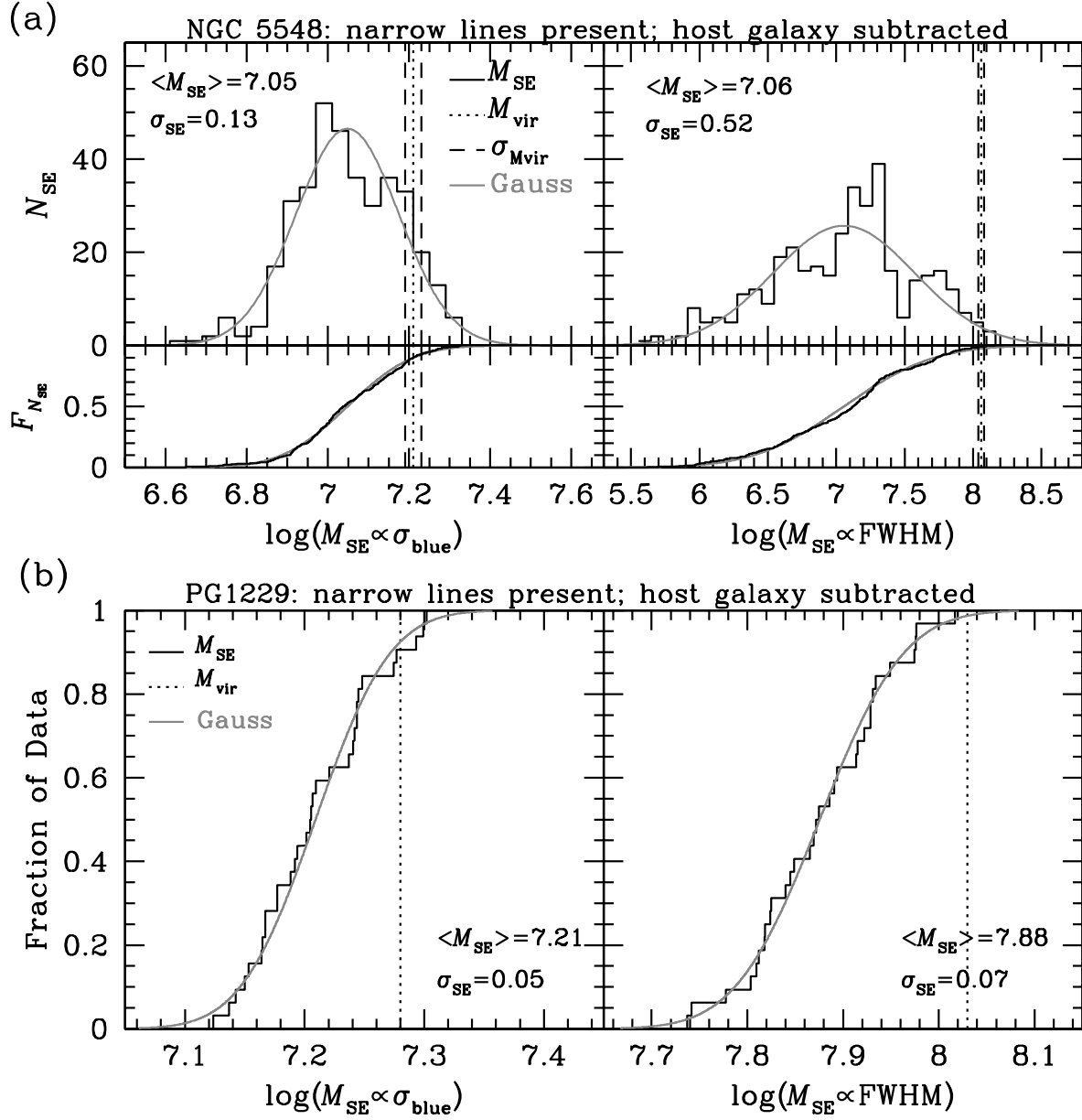


Fig. 9.— Same as Figure 4, except the narrow emission lines have not been removed from the spectra before measuring the  $H\beta$  line width. The host-galaxy contribution to the flux was removed before determination of the masses.

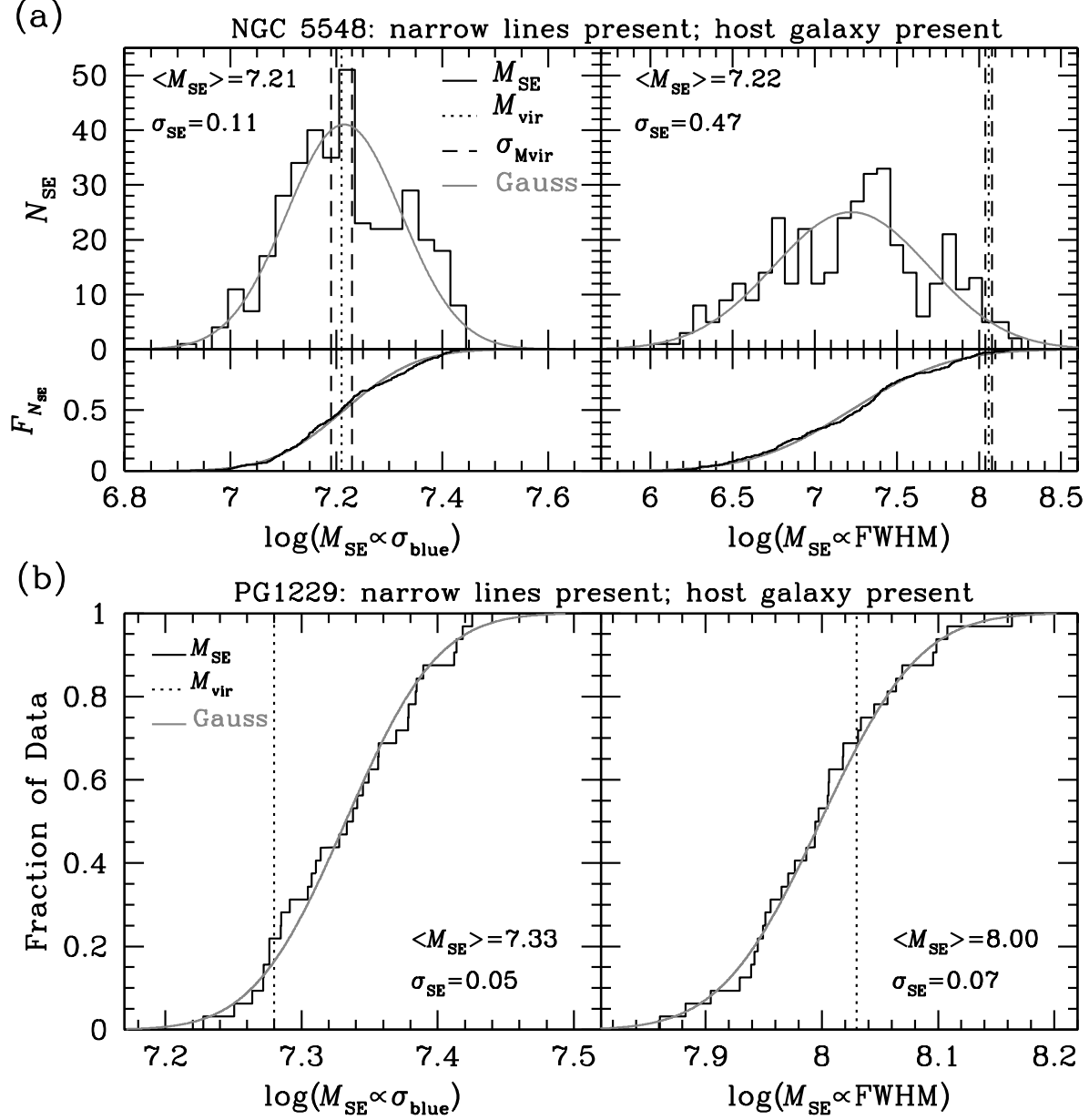


Fig. 10.— Same as Figure 4, except neither the narrow-line components nor the host-galaxy flux contribution have been removed before determination of the masses.

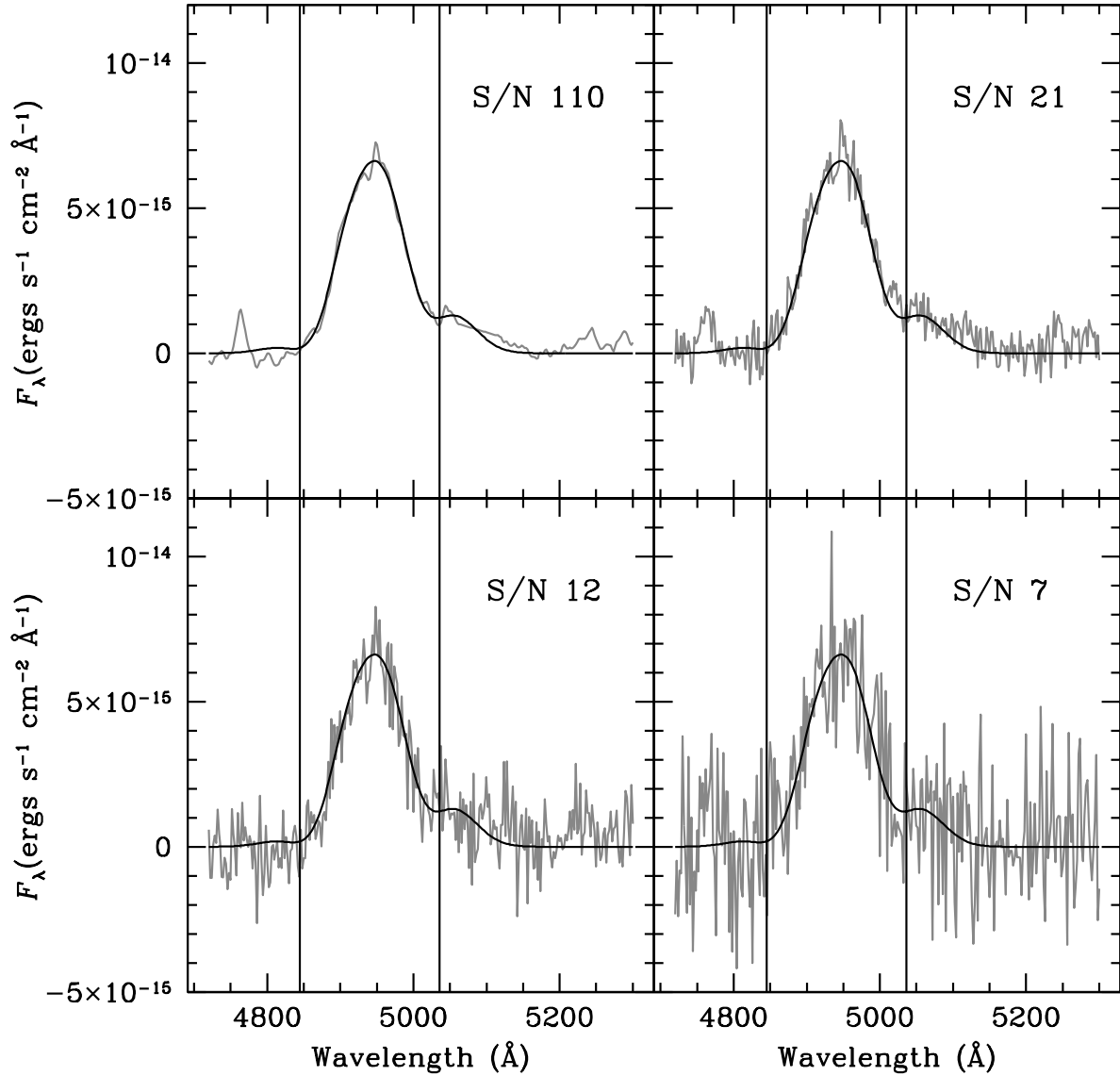


Fig. 11.— Example spectrum of NGC 5548 (top left) and three artificial degradations of the same spectrum with the resultant  $S/N$  labeled for each. The solid black lines are the Gauss-Hermite polynomial fits to each spectrum (gray lines) as described in §3.3.2. The vertical lines show the assumed boundaries of the broad  $H\beta$  line used for measuring the line widths from both the actual data and the Gauss-Hermite fits.

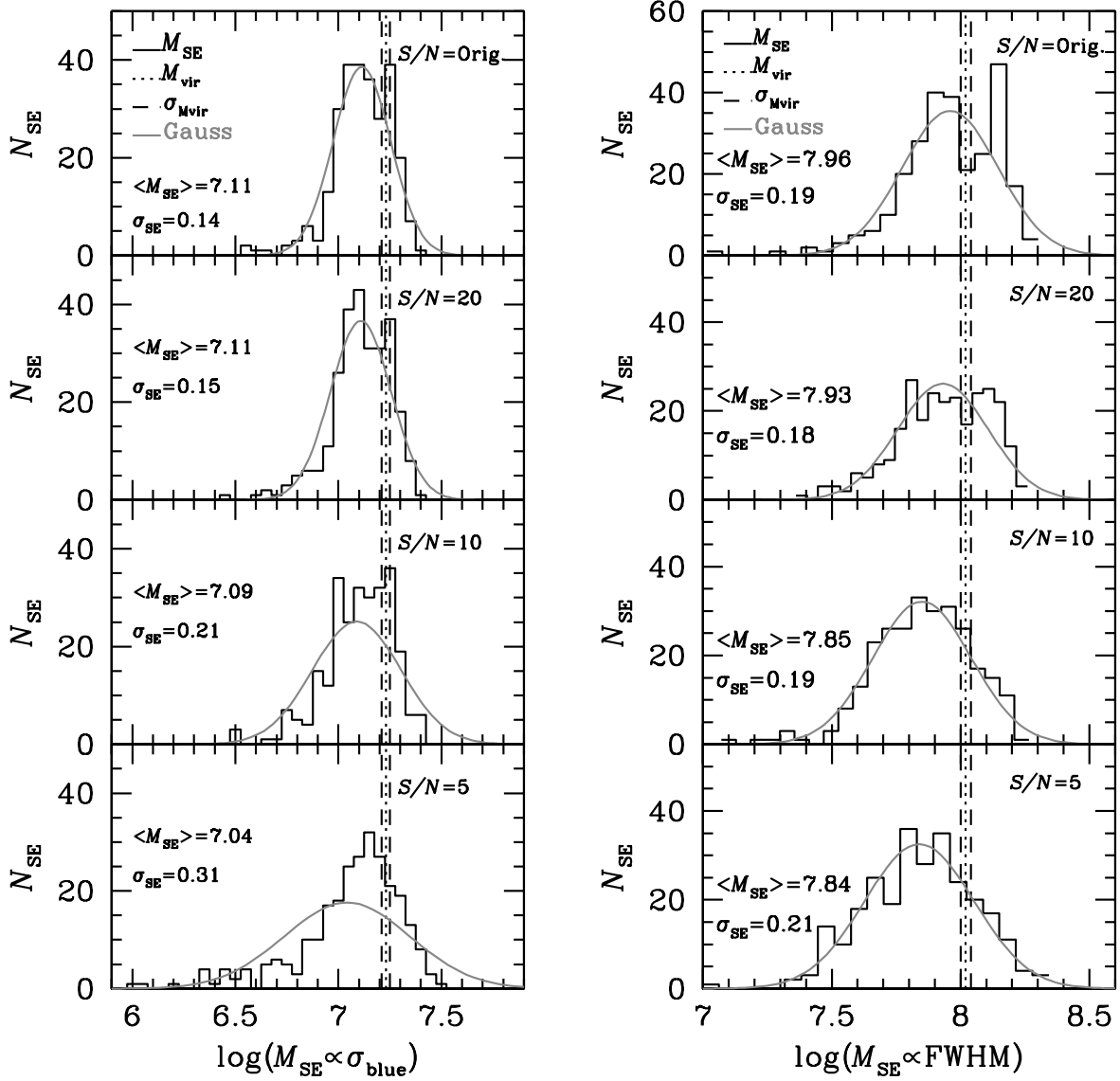


Fig. 12.— Virial mass distributions for the original and  $S/N$  degraded NGC 5548 Perkins data set, using line widths measured directly from the data. Virial masses are calculated in all cases by measuring the velocity dispersion of the broad  $H\beta$  emission from narrow line-subtracted spectra using  $\sigma_{blue}$  (left) and FWHM (right). All virial masses are calculated using a value of  $L_{5100}$  that has been corrected for host galaxy starlight.

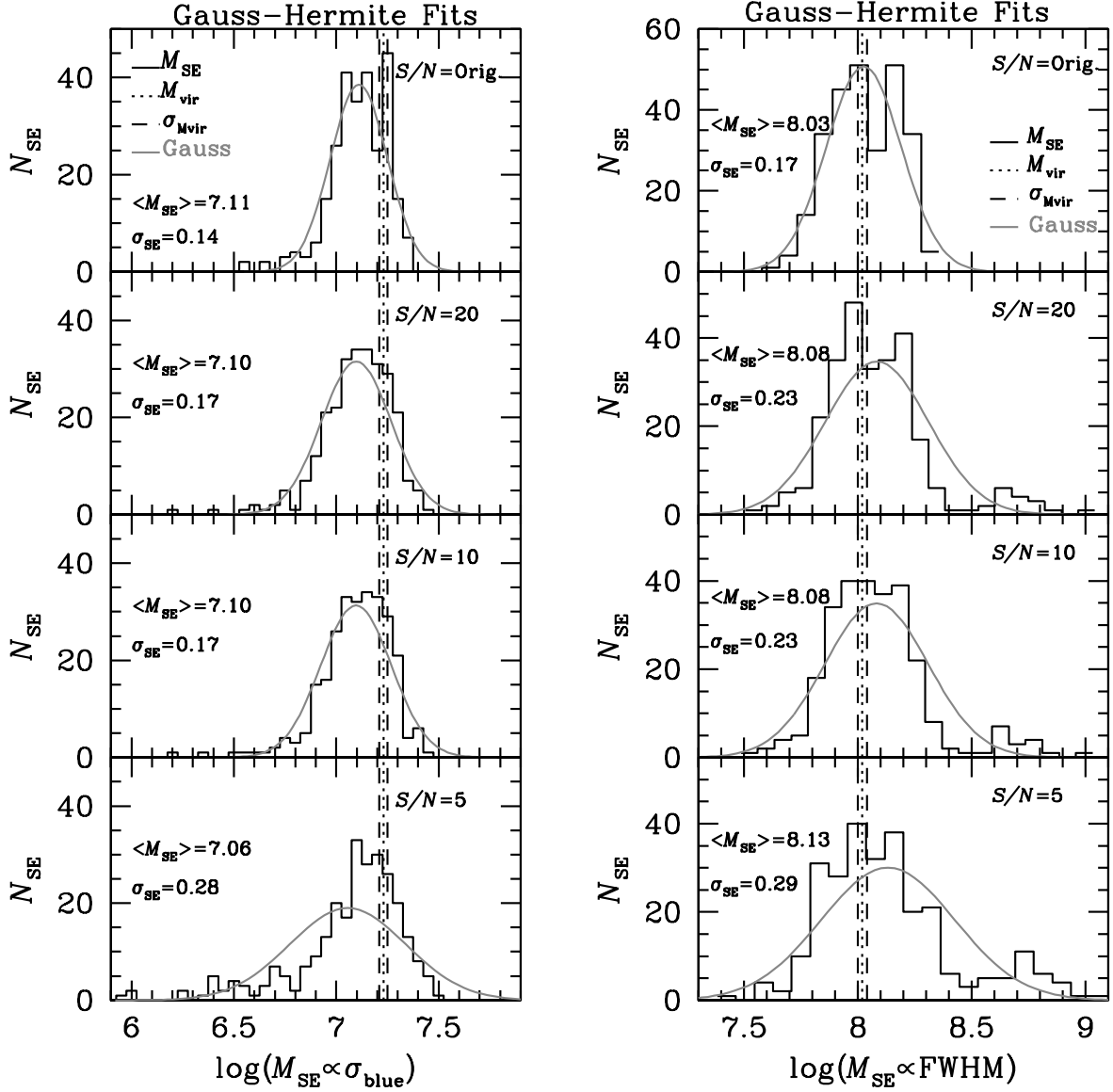


Fig. 13.— Virial mass distributions based on sixth order Gauss-Hermite polynomial fits to the original and  $S/N$  degraded NGC 5548 Perkins data set. Virial masses are calculated by measuring the velocity dispersion of the Gauss-Hermite polynomial fit to narrow line-subtracted broad  $H\beta$  emission line with  $\sigma_{blue}$  (left) and the FWHM (right). All virial masses are calculated with a value of  $L_{5100}$  that has been corrected for host galaxy starlight.

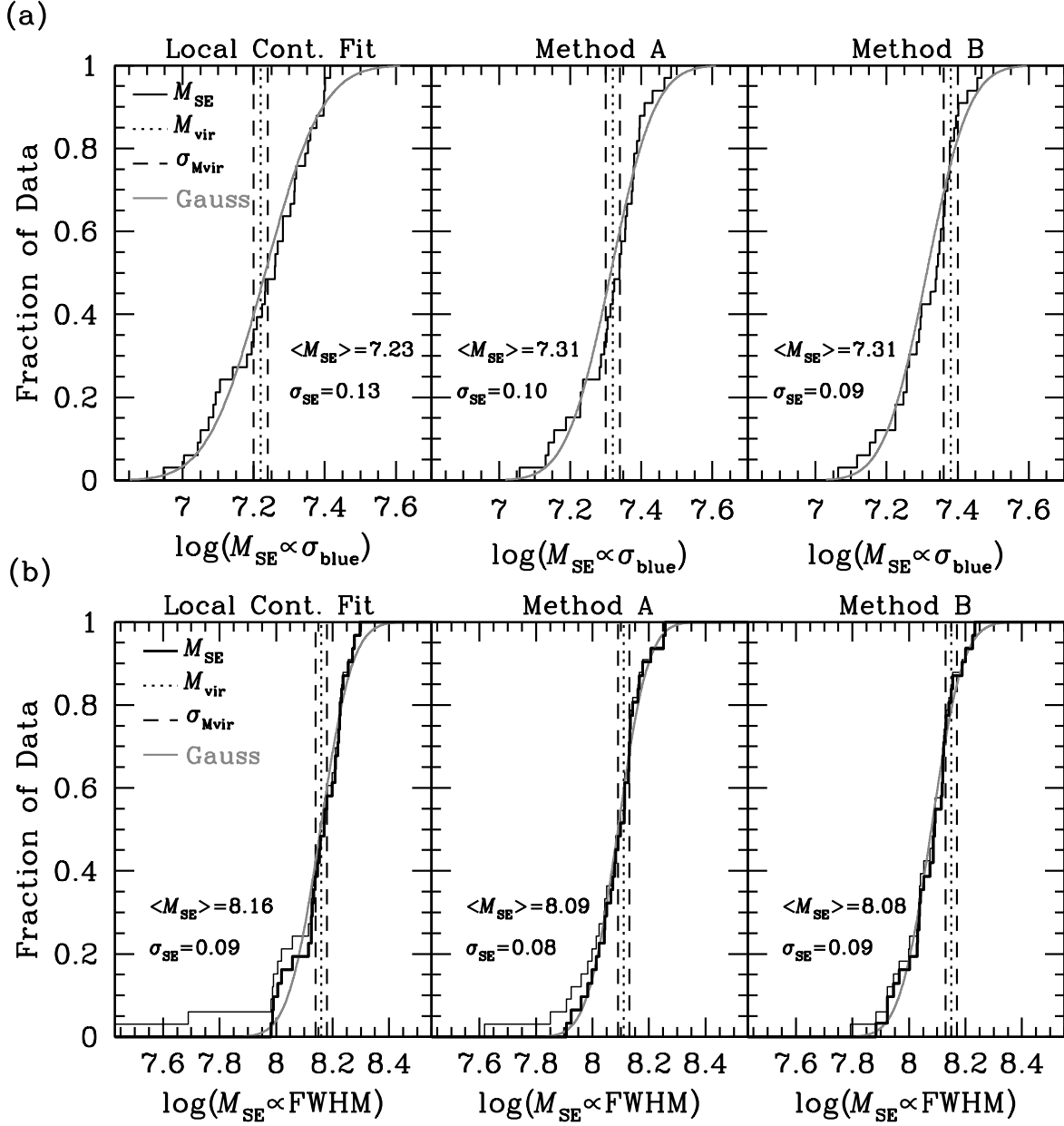


Fig. 14.— Cumulative distribution functions of NGC 5548 SE virial masses for decomposition data sets with  $\sigma_{blue}$  (a) and FWHM (b). The panels show virial mass distributions that have been calculated using a local continuum fit to the continuum underneath the  $H\beta$  line (left), spectral decomposition method A (middle), and spectral decomposition method B (right). Statistics listed in the bottom three panels do not include the outliers plotted in the thin black line, as described in §3.4.

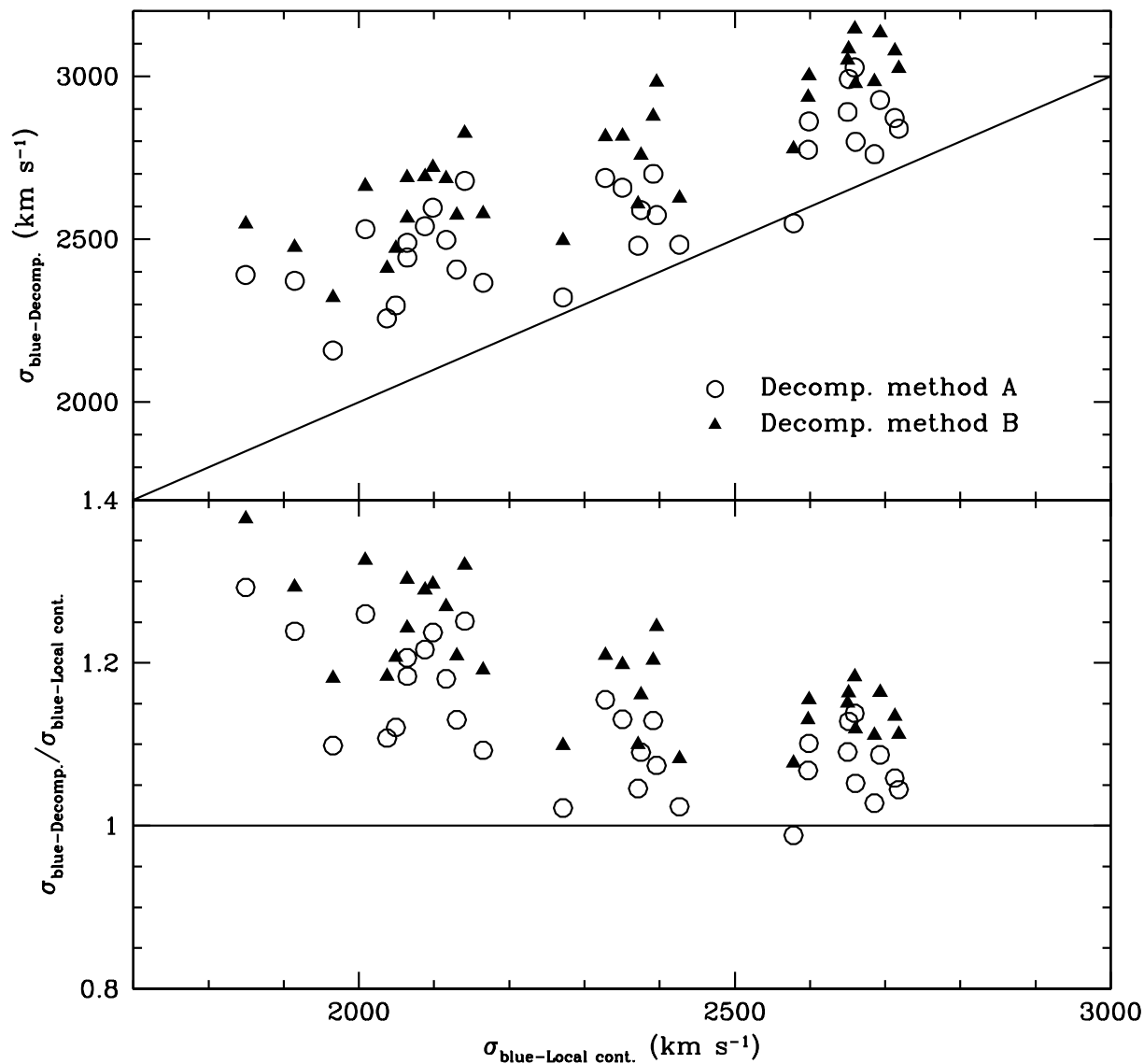


Fig. 15.— Comparison of the  $H\beta$  line dispersion measurements ( $\sigma_{\text{blue}}$ ) using the various techniques described in §3.4 to account for the continuum flux level under the emission line. The open circles represent the line width measurements using decomposition method A results, and the black triangles show results using method B. In the top panel, these values are plotted against widths measured using a local continuum fit, and the bottom panel shows the residuals with respect to the width from the local continua method. The solid black line in each panel shows a 1:1 correlation between the measured  $\sigma_{\text{blue}}$  values.

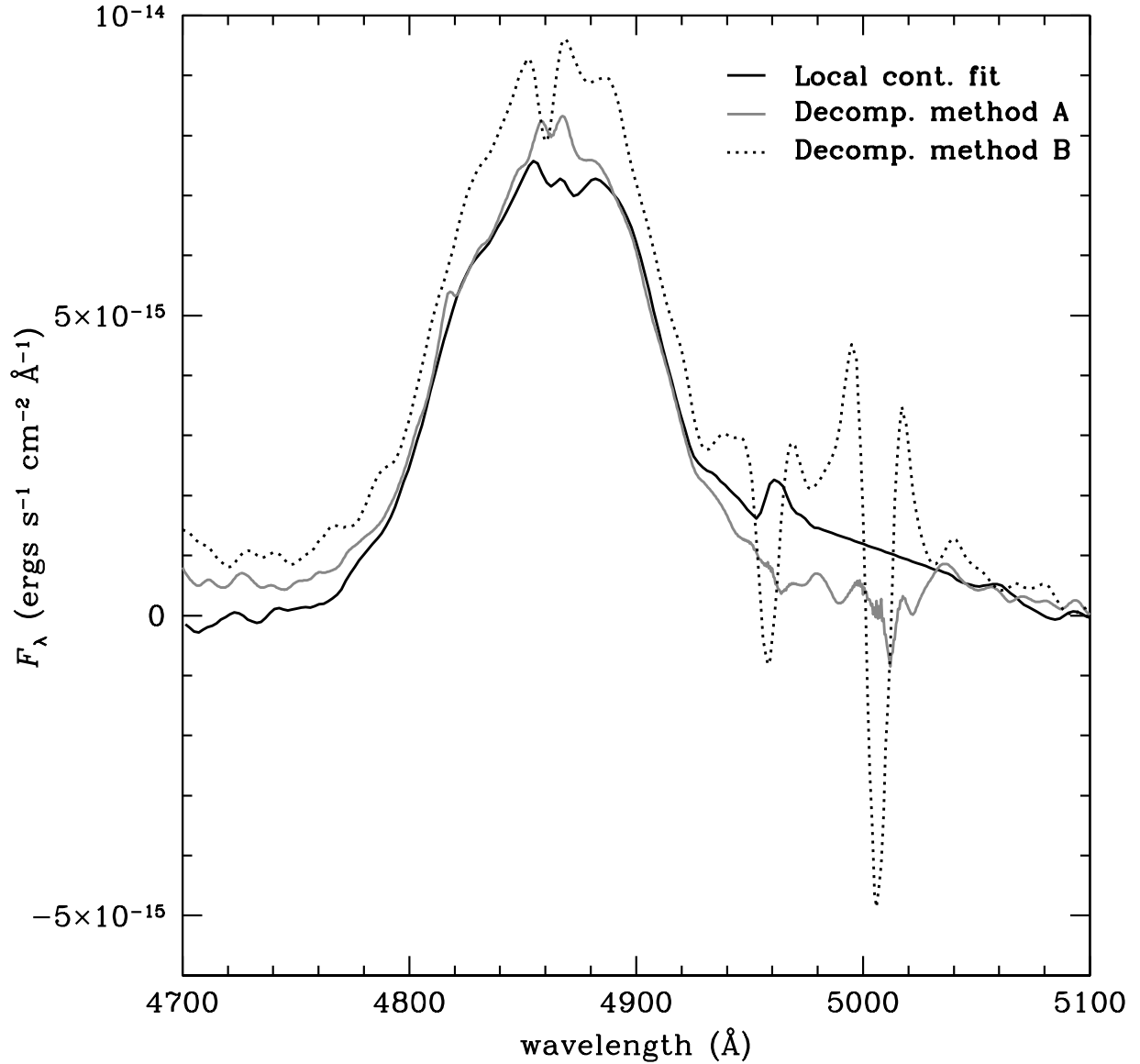


Fig. 16.— Mean spectra of NGC 5548 created using three different techniques to account for the continuum flux level under the H $\beta$  emission line (as described in §3.4). The black line shows the mean spectrum formed after simply fitting and subtracting a local linear continuum to each of the 33 spectra. The gray line shows the mean continuum-subtracted spectrum formed after deblending the spectral components from the same 33 spectra with method A, and the dotted line is the same, but for method B.



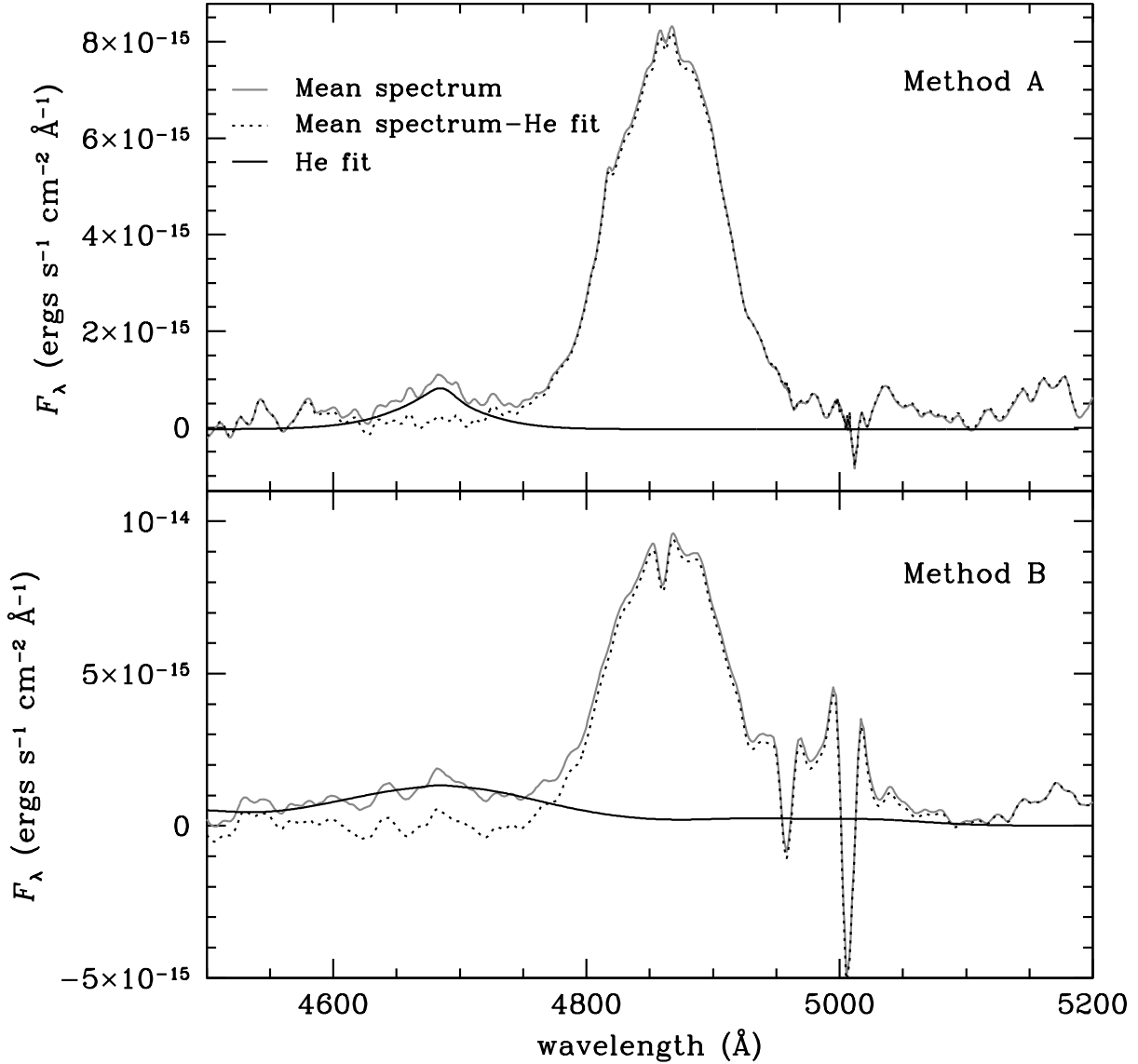


Fig. 17.— Mean spectra of NGC 5548 both before (gray lines) and after (dotted lines) subtracting the He II  $\lambda 4686$  emission line (black lines). The top panel show the results from decomposition method A, where the He II line was modeled assuming the line profile of  $H\beta$  is the same as  $H\alpha$ . The bottom panel shows the results from decomposition method B, where the He II line is fit assuming the same velocity width as the unblended He I  $\lambda 5876$  line.

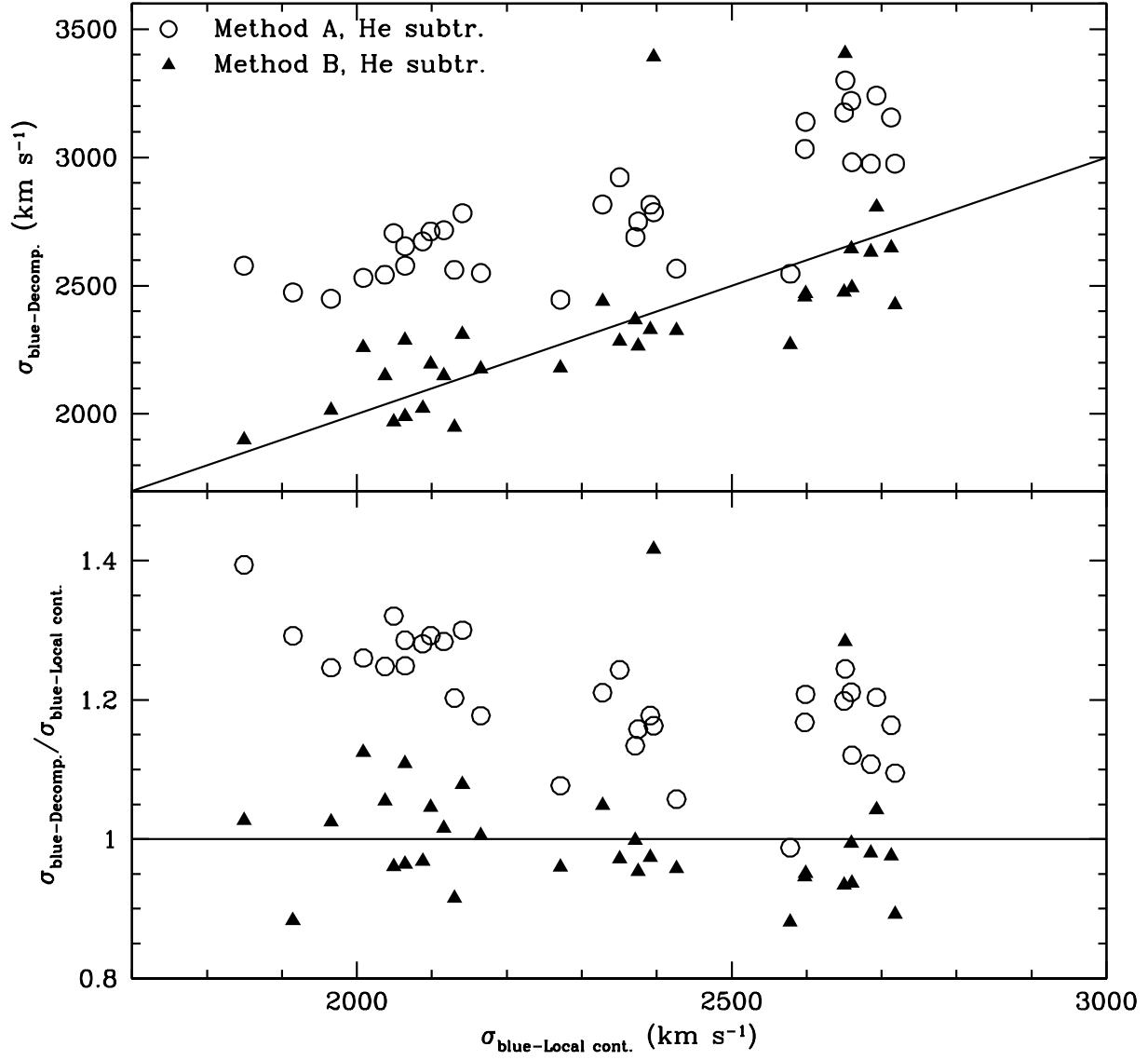


Fig. 18.— Same as Figure 15, except the He II  $\lambda 4686$  emission line has been subtracted from each of the spectra before measuring the H $\beta$  line dispersion ( $\sigma_{\text{blue}}$ ).

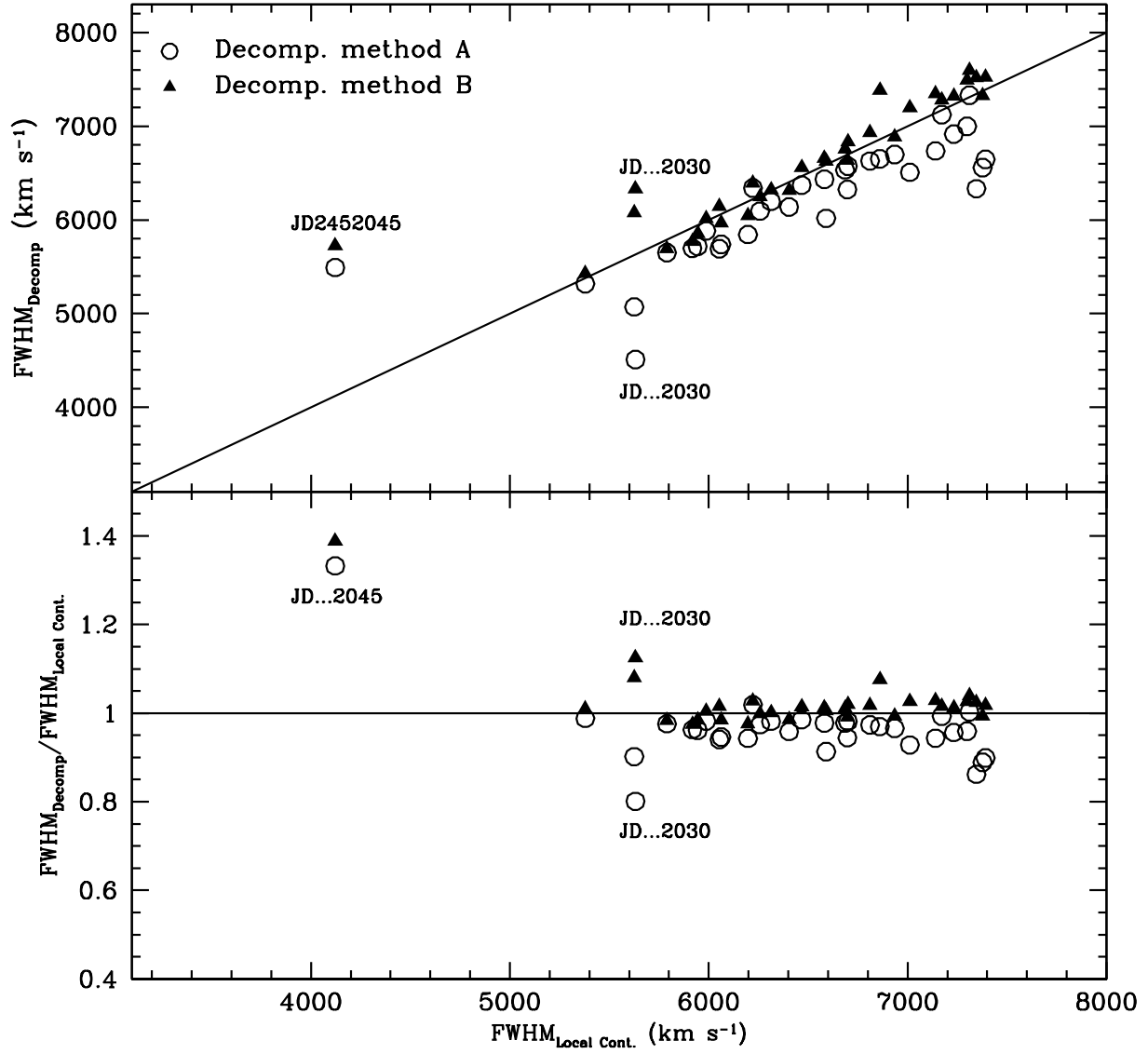


Fig. 19.— Same as Figure 15, except the width of the  $H\beta$  line is characterized here by FWHM rather than  $\sigma_{\text{blue}}$ . Outliers discussed in §3.4 are individually labeled by Julian Date.

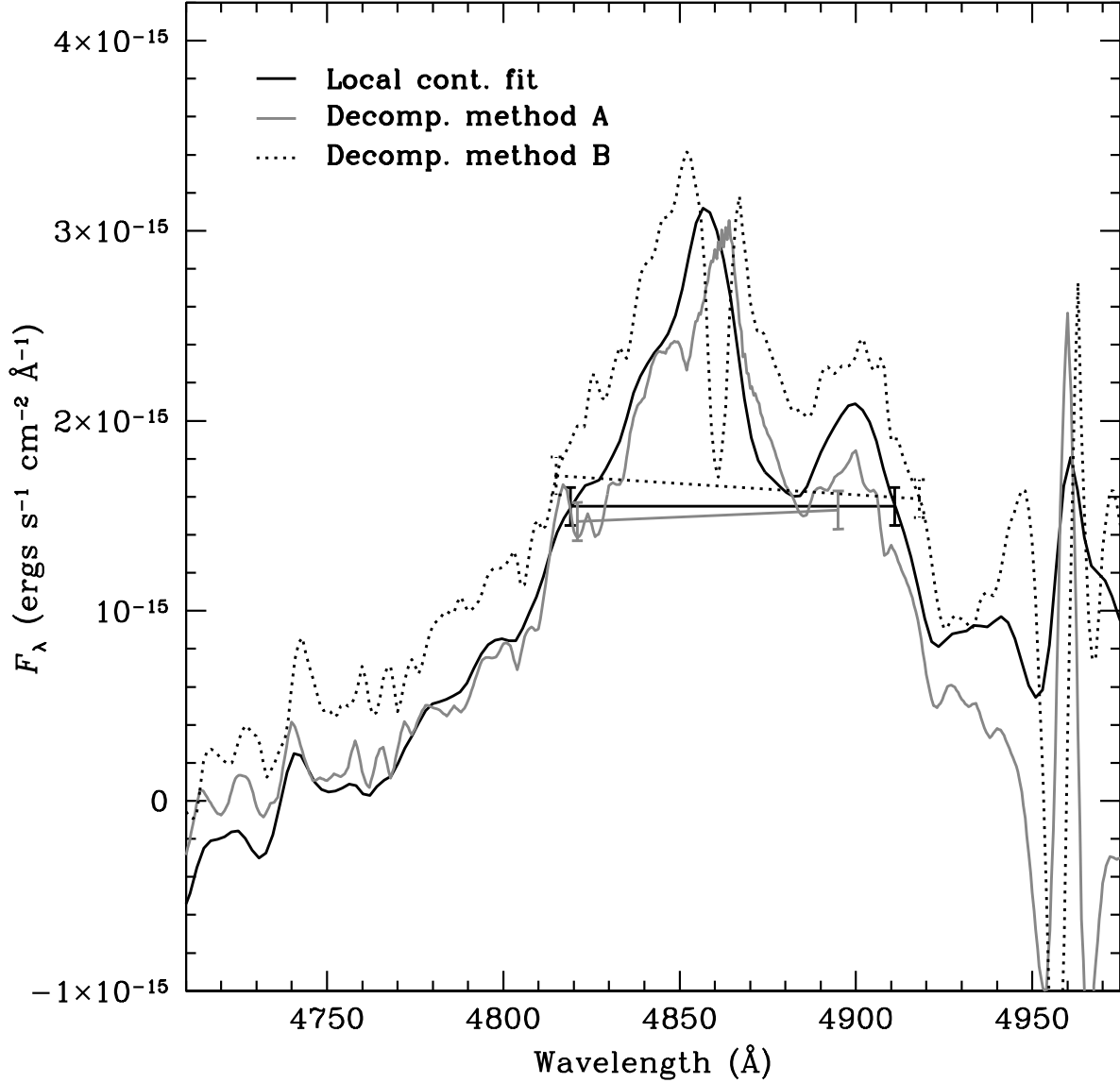


Fig. 20.— FWHM measurements of the  $H\beta$  broad line for JD2452030 using each of the three spectral analysis methods discussed in §3.4. The spectra shown here illustrate complications that arise when using FWHM to characterize a complex emission line structure, especially when the narrow emission-line components are not well-determined. The  $H\beta$  profile after subtracting a local continuum fit (black line) has FWHM= 5632 km s<sup>-1</sup>, the profile determined from decomposition method A (gray line) has FWHM= 4511 km s<sup>-1</sup>, and the profile from decomposition method B (dotted line) has FWHM= 6334 km s<sup>-1</sup>.